Advanced Engineering Materials

Atomic structures of precipitates in Al-Mg-Si alloys with small additions of other elements

--Manuscript Draft--

Manuscript Number:	
Full Title:	Atomic structures of precipitates in Al-Mg-Si alloys with small additions of other elements
Article Type:	Invited Review
Section/Category:	
Keywords:	aluminium alloys; precipitation; diffusion; precipitate structure; Al-Mg-Si alloys; transmission electron microscopy (TEM)
Corresponding Author:	Takeshi Saito Hydro Aluminium Sunndalsøra, NORWAY
Additional Information:	
Question	**Response**
Please submit a plain text version of your cover letter here. **If you are submitting a revision of your manuscript, please do not overwrite your original cover letter. There is an opportunity for you to provide your responses to the reviewers later; please do not add them here**.	Dear editors of Advanced Engineering Materials, Please find the enclosed manuscript entitled “Atomic structures of precipitates in Al-Mg-Si alloys with small additions of other elements” for a Review. The submission is based on an invitation to contribute a Review and agreed with an editor, Dr. Jos Lenders. Best regards, Takeshi Saito
Do you or any of your co-authors have a conflict of interest to declare?	No. The authors declare no conflict of interest.
Corresponding Author Secondary Information:	
Corresponding Author's Institution:	Hydro Aluminium
Corresponding Author's Secondary Institution:	
First Author:	Takeshi Saito
First Author Secondary Information:	
Order of Authors:	Takeshi Saito
	Eva A. Mørtsell
	Sigurd Wenner
	Calin D. Marioara
	Sigmund J. Andersen
	Jesper Friis
	Kenji Matsuda
	Randi Holmestad
Order of Authors Secondary Information:	
Abstract:	In Al-Mg-Si alloys, additions of only a few weight percent of Mg and Si enable formation of hardening precipitates during heat treatment. The precipitation is

	complex and influenced by chemical compositions and thermo-mechanical treatment. Structural analysis at the atomic scale has played an important role for understanding the Al-Mg-Si system. This review paper gives a summary of the influence of elements on the precipitate structures of Al-Mg-Si alloys at the atomic scale. The structures are modified by small additions of different elements, but all the encountered precipitates are structurally connected with the Si network, except for the main hardening phase β" which exhibit a partially discontinuous Si network. The influence of the selected elements (Li, Cu, Zn, Ge, Ag, Ni, Co and Au) are discussed in detail.

DOI: 10.1002/adem.((please add manuscript number))

Atomic structures of precipitates in Al-Mg-Si alloys with small additions of other elements**

By *Takeshi Saito*, Eva A. Mørtsell, Sigurd Wenner, Calin D. Marioara, Sigmund J. Andersen, Jesper Friis, Kenji Matsuda* and *Randi Holmestad*

[*] *Dr. Takeshi Saito, Corresponding-Author*
Hydro Aluminium, Research and Technology Development,
Romsdalsvegen 1, N-6601, Sunndalsøra, Norway
E-mail: (takeshi.saito@hydro.com)
Dr. Eva. A. Mørtsell
Norwegian University of Science and Technology (NTNU),
Alfred Getz' veg 2, N-7491, Trondheim, Norway
Dr. Sigurd Wenner, Dr. Calin D. Marioara, Dr. Sigmund J. Andersen, Dr. Jesper Friis
SINTEF Industry, Materials and Nanotechnology Department, Materials Physics Group, Høgskoleringen 5, N-7491 Trondheim, Norway
Prof. Dr. Kenji Matsuda
Graduate School of Science and Engineering for Research, University of Toyama, 930-8555, Toyama, Japan
Prof. Dr. Randi Holmestad
Department of Physics, Norwegian University of Science and Technology (NTNU), Høgskoleringen 5, N-7491, Trondheim, Norway

[**] *This article is partly written from contributions of PhD thesis of the authors, Saito, Mørtsell and Wenner written at the Norwegian Centre of Transmission Electron Microscopy (NORTEM), Norwegian University of Science and Technology (NTNU) through projects funded by KMB projects "The Norwegian-Japanese AlMgSi Alloy Precipitation Project" (193619) and "Smart alloy development for rolling and extrusion- RolEx" (219371) from Hydro Aluminium and the Norwegian Research Council. The authors also acknowledge the INTPART project "Norwegian-Japanese Aluminium Alloy Research and Education Collaboration" (249698) funded by the Norwegian Research Council for establishing the collaborations to write this article. S.J. Andersen acknowledges the SINTEF Hydro Fond project "Understanding and multi-scale modeling of early stage precipitation in age hardenable Al-Mg-Si alloys" at SINTEF. The Norwegian transmission electron microscopy infrastructure NORTEM (197405) has been used for TEM experiments and supercomputers at Sigma2/NOTUR (NN8068K) are used for DFT calculations.*

(In Al-Mg-Si alloys, additions of only a few weight percent of Mg and Si enable formation of hardening precipitates during heat treatment. The precipitation is complex and influenced by chemical compositions and thermos-mechanical treatment. Structural analysis at the atomic scale has played an important role for understanding the Al-Mg-Si system. This review paper

gives a summary of the influence of elements on the precipitate structures of Al-Mg-Si alloys at the atomic scale. The structures are modified by small additions of different elements, but all the encountered precipitates are structurally connected with the Si network, except for the main hardening phase which exhibit a partially discontinuous Si network. The influence of the selected elements (Li, Cu, Zn, Ge, Ag, Ni, Co and Au) are discussed in detail)

1. Introduction

Al-Mg-Si alloys (classified as 6xxx series alloys) are widely used for industrial purposes all over the world. As the need for recycling friendly, lightweight materials is increasing, the demand for high quality, multi-purpose aluminum alloys has increased correspondingly. The industrial applications range from the transport sector including automotive and marine industries to buildings and constructions. The reason for their wide applicability is the attractive properties of the Al-Mg-Si alloys, providing medium strength, good formability and corrosion properties, which are highly suitable in many industrial applications.

Precipitation hardening in the Al-Mg-Si system was first discovered almost a hundred years ago [1]. Since this groundbreaking discovery, a vast number of different alloys has been developed for targeted applications. Adding only a few weight percent of Mg and Si enables the formation of hardening precipitates, when the alloy is subjected to heat treatment. Precipitation is a complex diffusion limited phenomenon in the solid state, depending on chemistry and thermo-mechanical processing, which need to be tightly controlled during industrial processing. Tremendous research efforts (for examples, see refs. [2-21]) have been devoted in order to understand the influences of chemistry and thermo-mechanical processing on solute clustering, precipitation and consequent mechanical (and other) properties.

There has been tremendous progress in analytical and computational tools for materials characterization, allowing structural analysis down to the nanoscale level. This has

shown to play an important role for understanding and further development of aluminium alloys including the Al-Mg-Si system. It has become more and more clear that it is necessary to investigate the precipitate structures at the atomic scale in order to achieve the desired macroscopic properties of the alloys [22-31]. Consequently, by achieving a complete understanding of the precipitate structures, it should be possible to tailor alloy chemistry and thermo-mechanical treatment to achieve desired macroscopic properties for a certain application. An illustration of the different length scales in alloy design, from macroscopic products to atomic resolution transmission electron microscopy (TEM) is given in Figure 1.

In this review article, we focus on summarizing the effects of small additions of selected elements in Al-Mg-Si alloys. As will be seen, the elements have strong influences on atomic structure of the precipitates, on morphology, as well as on stability. Recent developments in characterization tools, in particular aberration corrected TEM, have greatly contributed to enhanced understanding. The methodology of the structural analysis is given in appendix A as short descriptions. In chapter 2, effects and roles of elements in the general aluminium alloys will be described. In chapter 3, the detailed precipitate atomic structures encountered by the main alloying elements Mg and Si will be described, as well as the aspects connecting to nucleation and growth of the precipitate phases in Al-Mg-Si alloys. Chapter 4 will be the main section describing how additional elements influence the precipitate atomic structures. A summary and perspectives for further research will be written in Chapter 5.

2. Behavior of solute elements in aluminum

The role of the alloying elements depends on thermodynamics and diffusion as well as solubility, interactions and binding to vacancies and the other elements. All these properties may affect the formation of primary phases and dispersoids, grain refinement, precipitation and so on. An overview of categorized roles for each element known to affect the properties

of aluminum alloys is shown in Figure 2. The roles of the different elements are summarized in the following sections, starting with the effect of vacancies.

2.1. Vacancies and binding

Quenched-in vacancies, which occur upon cooling from the homogenization temperature, play an important role during the nucleation stages of the hardening phases [32, 33]. Coarse distributions of inhomogeneous precipitates can be the result of dislocation loops, which form as vacancies assemble into clusters [33]. This effect can be minimized by adding a higher amount of solute to the alloy, or by adding solutes with a higher affinity to vacancies. With a few exceptions, the vacancy affinity of chemically similar solute elements in aluminum generally increases with atomic size [23, 34]. Figure 3 illustrates DFT calculations of interaction energies between a number of solute elements and between the solutes and a vacancy (vacancies will hereafter be denoted by X). The interaction energies are plotted as a function of inter-atomic distances in fcc aluminum, up to two unit cell lengths (0.81 nm). The two shortest distances that are plotted in Figure 3 are the nearest neighbor distance, 0.286 nm, and the smallest periodic extent of one unit cell, 0.405 nm, respectively. Na, Ge and Ag are the three elements which should have the highest affinity to vacancies, while two vacancies next to each other, X-X, is the most unlikely combination. The same tendency was also reported in refs. [35, 36]. Germanium in particular is known to accelerate the precipitation kinetics in 6xxx Al alloys, which is in good agreement with a low Ge-X interaction energy. See appendix A or ref. [37] for more details.

2.2. Elements forming primary phases and dispersoids

Fe is an element forming primary phases under solidification in aluminum alloys including the Al-Mg-Si system. The Fe containing primary phases are commonly referred to as α-$Al_{15}(Fe,Mn)_3Si$, β-Al_5FeSi and π-$Al_8FeMg_3Si_6$ in Al-Mg-Si alloys, for example in refs.

[39, 40]. The fraction of α and β phases is often addressed due to its effect on the ability of hot deformation, e.g. extrudability. The transformation β -> α occurs during homogenization [41]. It is known that Mn is an element inducing additional transformations to the α phase [42]. Mg and Si are responsible for the primary phase which can form Mg_2Si during solidication in Al-Mg-Si alloys. When Mg and Si alloy contents are below the maximum solubility of Mg_2Si, the Mg_2Si phase is dissolved during high temperature treatments associated with alloy processing concerning formation of hardening metastable precipitates, which is the main focus in this paper, see details in chapter 3.

Some additional transition elements, like Mn, Cr, Zr and Sc, lead to dispersoids in Al-Mg-Si alloys during homogenization. This plays an important role for the nucleation and growth of grains during hot deformation (e.g. extrusion and rolling) for controlling microstructure and improving mechanical properties [43, 44]. Mn and Cr are the most commonly known elements for dispersoid formation and are often referred to as α-Al(Fe,Mn,Cr)Si dispersoids [45]. Zr is an element well known to form coherent Al_3Zr dispersoids in aluminum alloys e.g. in Al-Zr binary alloys [46] and Al-Zn-Mg alloys [47]. The coherent Al_3Zr dispersoids lead to high strength and good high temperature stability. However, due to the presence of Si in Al-Mg-Si alloys, incoherent $Al_3(Zr,Si)$ dispersoids dominantly form during homogenization [48]. Sc is also known to bring about incoherent dispersoids $Al_3(Sc,Si)$ in Al-Mg-Si alloys due to the presence of Si [49]. The Zr and/or Sc containing incoherent dispersoids act as recrystallization inhibitors in Al-Mg-Si alloys [48-50]. Hf is a transition element with similar behavior, regarding formation of dispersoids in aluminium alloys [51, 52].

In general, the transition elements behind formation of primary phases and dispersoids have no direct influence on precipitate atomic structures in Al-Mg-Si alloys. However, the dispersoid formation influences precipitation to some degree. For example, coarse Mg_2Si particles preferentially nucleate on dispersoids under cooling after solutionizing or extrusion

and the potential strength increase is reduced. This is known as quench sensitivity [53, 54]. This phenomenon is likely to happen in denser, high strength alloys, like AA6082 [55]. It is also important to note that the formation of primary phases and dispersoids consume some Si, which reduced the amount of "available" Si for formation of metastable precipitates [56, 57], which has been observed to be linked to precipitate free zones around dispersoids [55]. See also section 2.4 for further information.

2.3. Elements for grain refinement

In general, grain refinement is crucial for reducing defects during casting and solidification. For this purpose, Ti and B are well known elements. It is well established that TiB_2 particles with an Al_3Ti interface layer formed by a peritectic reaction act as nucleation sites for grains in aluminum alloys. This effect is mainly due to the high coherency of the Al_3Ti interphase (interface layer) with fcc aluminium. For example, ref. [58] is a study demonstrating this on the atomic scale. Some transition elements work as nucleation sites of grains during solidification under their peritectic reaction in aluminum alloys [59]. The final grain sizes and structures are influenced by the hot deformation processes, like extrusion or rolling. Although these grain refining elements have no direct influence on the precipitate atomic structures, grain size is an important factor also concerning precipitation of metastable precipitates considering how diffusivity depends on the elements in the aluminum matrix [60, 61].

2.4. Elements detrimental to precipitation

To optimize the benefit of the solute elements it is important that they contribute to homogeneous precipitation in the best way, forming efficient hardening phases with optimum sizes and distributions. Some Si will always be locked up in stable (primary or secondary) phases. Also, Mg and Si will form coarse Mg-rich phases like β' and β, altering the effective

Mg/Si ratio for the hardening phases. In both cases the beneficial precipitates are deprived of solute. Over the years, industry has learned to compensate for the effects, minimizing undesirable changes in the macroscopic properties. While the inclusion of Si in primary phases and dispersoids is taken into account, many other elements exist as more or less inadvertent impurities which can lock up solute elements, with negative or no significant influence to the alloy properties. The following gives a few examples.

Calcium, which is chemically similar to magnesium, forms the phase Al_2CaSi, which is isostructural to the U1-Al_2MgSi phase [62]. Contrary to the U1 phase, the Ca-containing equivalent is not coherent with the Al matrix and grows as large, stable particles with no hardening potential [63].

Hafnium is known to form belt-shaped Si_2Hf precipitates in Al-Si casting alloys [52, 64], showing high temperature stability and thus locking up Si throughout the SHT. Compared to the high content Si, the Si_2Hf hardening potential at room temperature is much lower than that of the smaller coherent β" phase. Therefore, Hf may be considered detrimental to the strength of Al-Mg-Si alloys at room temperature because of reduced precipitation hardening. In a similar manner, any element from the periodic table may be detrimental to precipitation if they are added in an amount that surpass the solubility limit for a stable phase that includes Si or Mg.

3. Precipitate phases in 6xxx alloys

After homogenization, solution heat treatment or other high-temperature (> 400°C) treatments associated with alloy processing, Mg and Si are dissolved in the Al matrix. With most wrought Al-Mg-Si alloys, the amounts of Mg and Si are below the maximum solubility limit (Al-Mg_2Si pseudobinary phase diagram can be found elsewhere e.g. ref. [65]), which means that all Mg, and all Si that does not participate in dispersoid formation, is dissolved. During artificial aging, the alloy goes through several phase transformations, from a

supersaturated solid solution (SSSS) to phases that are thermally stable and insoluble at the given aging temperature – i.e. nucleation, transformation and growth. Nucleation is driven by a negative free energy change, while the rate of transformation and growth is determined by interfacial energy and volume free energy. During growth of precipitates, interfacial energy changes with respect to crystal structure and/or composition of precipitates surrounded by the Al matrix, and several precipitate phases are encountered from metastable precipitate phases having a high coherency with the Al matrix to incoherent equilibrium phases.

The precipitation sequence of the Al-Mg-Si system is commonly written [2, 4]

$$SSSS \Rightarrow Atomic\ clusters\ [3, 10, 13] \Rightarrow GP\ zones\ [24] \Rightarrow \beta''\ [27, 66] \Rightarrow$$
$$\beta'\ [67, 68], U1\ [62], U2\ [69], B'\ [70] \Rightarrow \beta\ [71, 72], Si\ [73] \quad (1)$$

where the post β" phases, U1, U2 and B' are also known as Type A, Type B and Type C, respectively [4, 74]. An overview of the structural unit cell models of all the ordered metastable precipitate phases in Al-Mg-Si alloys is shown in Figure 4 and Table 1.

The main hardening phase, responsible for the strength of most age hardenable 6xxx alloys in use, is the fully coherent β". This and the other hardening phases in the sequence are formed as needle/rod-shaped particles, with lengths from a few nanometers to a few hundred nanometers, and cross-sectional size from one to some tens of nanometers. The main coherency and growth direction is along <001>Al for all phases except the stable ones, giving them a lattice parameter of a_{Al} = 0.405 nm in one of their crystallographic directions. For a particular alloy the phases formed will depend on composition and on the thermo-mechanical treatment, but the local conditions, such as grain boundaries, dislocations introduced during stretching or rolling, dispersoids, etc, will also contribute.

The structure and composition of β" have been widely discussed during the last twenty years. Firstly, the crystal structure and the composition Mg_5Si_6 were demonstrated [22, 66].

Through further development of characterization methods, incorporation of Al in β” – $Mg_5Al_2Si_4$ was proposed [27, 28]. The Al incorporation has also been observed by several atom probe tomography (APT) studies [3, 19, 75, 76], which has been accepted in recent years. Some density functional theory (DFT) studies show possible Mg–Al compositional fluctuations, $Mg_{(6-x)}Al_{(1+x)}Si_4$ ($0 \leq x \leq 2$) [77]. Furthermore, by atomic resolution energy dispersive X-ray spectroscopy (EDS), it has recently been demonstrated [78] that Al is incorporated in β”. Such observations of Al incorporation and calculated compositional fluctuations cannot explain the stability of Si–Si bonds proposed as the "Si nanopillars" based on Mg_5Si_6 in ref. [79]. This argument and discussion can be found in detail e.g. in ref. [27]. Incorporation of low amounts of Cu [80] or Zn [81] in β” has also been observed. However, the β” compositions are not significantly influenced by Cu and Zn. It has also been discovered different stacking variations of the "eye like" β” molecules, denoted β”–eyes (see Figure 4), in Li or Ge containing alloys [37, 82]. See details in Chapter 4. According to ref. [83], twelve different orientations exist between Al and β”.

All the post-β” phases consist of atomic columns of metal elements in-between triples of Si columns, which form a Si-network that is hexagonal in projection, originally proposed by Andersen [84], and later expanded upon by [29, 62]. This Si network has a projected lattice spacing of about 0.4 nm, equal to the lattice parameter of Al, and the hexagonal bases oriented along the <100>Al or <510>Al directions, depending on the phase precipitated. All the Si atoms of the network act as vertices for alternating pyramids and tetrahedra spanning the length of the precipitate. In Figure 5, these structural features are depicted for the U2 phase, here with pyramids connected edge to edge along its extension. Notice that all Si atoms can always be assigned to a set of empty square-based Si pyramids that are connected either base-base (like in diamond Si, the U1 phase and the β-Mg_2Si phase), edge to edge or face to face. For example, in β, 8 Mg atoms surround the Si octahedron that is defined by atoms of the faces. The Mg atoms define a simple cube outside the triangular faces, on the diagonals of the

cell. The Si-Si edges are 0.449 nm in β, while corresponding edges in diamond Si are only 0.384 nm. In the diamond structure there are only Si atoms found outside half the triangular faces (i.e. four). In order to minimize the formation enthalpy, pyramids are typically occupied by Al atoms and tetrahedra by Mg atoms [29]. A special triangular geometry is included in e.g. the B' phase, and may include Al or Cu atoms. Any site, including the Si network sites, may be occupied by certain foreign metal atoms (indicated in Figure 2).

Due to its full coherency with the Al matrix, the main hardening phase β" does not contain a perfect Si network such as the phases mentioned above, but exhibit a partially discontinuous Si network, with "stacking faults" on planes perpendicular to the <001>β" direction. The C phase in Al-Mg-Si-Cu alloys (see section 4.2 and Figure 7) comes close to such a realization, hosting a <100>Al-oriented Si network, but C precipitates always have a short, semi-coherent interface.

The discrete phases from the precipitation sequence do not tell the whole story. The projected triangular elements of the Si network (the columns of alternating pyramids and tetrahedra) do not necessarily repeat: They may be stacked disorderly as long as they obey a few simple rules [29, 85]. Precipitates which are composite of such "building blocks" without any repeating unit cell are referred to as disordered. Disordered phases may contain fractions of the ordered phases shown in the precipitation sequence (e.g. see section 4.2), and retain the same orientation relationship with Al, always having a repeating structure along the main growth direction (<001>Al).

4. Elements participating in metastable precipitation

4.1. Lithium (Li)

Li has a relatively high solid solubility in aluminum, and because of its low atomic number, Li will reduce the density of the alloy [86]. An improvement to the age hardening behavior of Al-Mg-Si alloys can be achieved by adding small amounts of Li. It has been

documented that Li enters the structure of the hardening phases, while no significant changes are made to the precipitation sequence [82, 87]. However, better thermal stability for the Li-added alloy as compared to a Li-free reference was reported. An example of precipitate microstructure and a precipitate cross section, as observed by TEM, is given in Figure 6.

Since Li does not change the precipitation sequence, the main hardening phase is still β”. However, it has been found that it is energetically favorable for Li to enter atomic columns normally occupied by Mg in β”. Experimental images with atomic number contrast acquired by high angle annular dark field scanning TEM (HAADF-STEM) confirm that Li in particular prefers the Mg3 sites in β”. The Mg3 site is the most probable to be occupied by Li atoms according to density functional theory calculations, although it is also deemed energetically favorable for the element to occupy Mg1 and Mg2 sites [82]. The low intensity of Mg3 sites in β” can be observed in Figure 6 (b), indicating a relatively high amount of Mg being substituted by Li. Although the main hardening precipitate phase is β” for such alloys, a higher frequency of stacking variations of the β”-eyes occurs. In particular, stacking faults throughout the entire precipitate cross section are observed, see Figure 6 (b). These stacking variations are denoted β_2” and will be further discussed together with β_3” in the germanium section, section 4.4, where they are considered even more likely to form.

In a surface study conducted by X-ray photoelectron spectroscopy (XPS), in-situ heating experiments showed that Mg prefers to migrate to grain boundaries at elevated temperatures, while Li was detected across the entire specimen surface [88]. Prior to annealing, the surface abundance of the alloying elements was too low to be detected. The migration of Li to the sample surface also occurred at a significantly higher temperature than Mg [88]. This should be kept in mind, as the available solute for precipitation will decrease close to the material surface.

4.2. Copper (Cu)

Cu is the main alloying element in 2xxx series alloys. In Al-Mg-Si alloys, Cu is an element increasing peak hardness, which is correlating with increase in number density and volume fraction of precipitates. Addition of Cu ($\sim$ 0.4 wt%) alters the precipitation sequence of Al-Mg-Si system as follows [89, 90]:

$$SSSS \Rightarrow Atomic\ clusters\ [3, 10, 13] \Rightarrow GP\ zones\ [24] \Rightarrow$$
$$\beta''\ [27, 66], L\ [90], C\ [91], QP\ [91], QC\ [67, 92] \Rightarrow \beta'\ [67, 68], Q'\ [73, 89, 93] \Rightarrow Q\ [23, 94] \quad (2)$$

This redistribution of solute suppresses the formation of β" and forms different types of precipitates. The L phase has a lath morphology and is a disordered structure [90], showing compositional variations [95]. It has been demonstrated [96] that the L phase has a good thermal stability, and a correspondingly slower over-aging. In addition, the L phase forms in Mg-rich Cu containing alloys with high Mg/Si ratios (>2) [96]. It was also demonstrated that the Mg/Si ratio plays an important role for formation of L phase [97, 98]. The C phase has a plate shape morphology with a monoclinic unit cell [91]. Both L and C phases are elongated along <001>Al and have a habit plane <100>Al, and are believed to be precursors of the Q' phase. The QP and QC phases have been claimed to be hexagonal and structurally connected with the Q' phase [67, 92]. The observed $\sim$ 0.4 nm periodicity of QP could be a disordered phase connected with the Si network and $\sim$ 0.7 nm of QC could be the β'_{Cu} phase (see the detailed description of β'_{Cu} below in this section), which were partly discussed in [90]. The Q' phase is isostructural to the B' phase, having Cu replaced with Al, and is encountered in over-aged conditions [90]. Several variations of orientation relationships of Q' precipitates were observed with respect to the aluminium matrix [99, 100]. It was also observed that Cu atoms are segregated at Al matrix sites along the main interface of Q' precipitates [101]. The Q phase is the equilibrium phase with the composition proposed as $Al_3Cu_2Mg_9Si_7$ [23]. There

are also several reports showing slightly different Q compositions, $Al_4Cu_2Mg_8Si_7$ [94], $Al_5Cu_2Mg_8Si_6$ [102], within $Al_xCu_2Mg_{12-x}Si_7$ [94]. It has been suggested possible Cu–Mg compositional fluctuations in the Q phase by DFT and APT studies [103, 104] and also recently by energy dispersive X-ray spectroscopy (EDS) imaging with atomic resolution [78]. A recent study has observed θ', a typical precipitate phase in 2xxx series alloys, together with β" and Q' phases when the Cu contents increase up to 4.5 wt% in an Al-Mg-Si alloy [105]. Figure 7 and Table 2 give an overview of the structural unit cell models of metastable precipitate phases in Cu containing Al-Mg-Si alloys.

Even when added in small amounts (~ 0.1wt%), Cu causes increase in number density of precipitates, as was observed in a 6060 alloy [106, 107]. It has been demonstrated that low additions of Cu make β" partly disordered [108]. Figure 8 gives an example showing coexistence of structurally perfect β" and disordered parts in the same precipitate needle cross section. Cu atomic columns were found in the disordered part. The disordered precipitates are composed of local atomic column arrangements consistent with fragments of different types of metastable precipitates in the Al-Mg-Si(-Cu) system. This exists on the common near hexagonal Si-network (see Chapter 3). The fragments, which are needle-shaped as they span the entire length of a precipitate, are commonly observed in disordered precipitates, also identified in Li, Zn and/or Ge containing Al-Mg-Si alloys (see each section). All Cu atomic columns can be categorized by two different local atomic column arrangements connected to the Si-network [108]; *in-between* the Si network columns (existing in Q' and C phases) and *on* the Si-network (existing in the isostructural Ag containing β' phase), see Figure 7. In this paper, the former is called "Q'/C phase like" local atomic column arrangement, while the latter is called "β'_{Cu} phase like". Those observations were also made in Cu containing disordered precipitates in a recent study [109]. Even for the disordered structures with Cu, the column arrangements with the Si-network follow the same rule [29, 85], see Chapter 3. A

recent paper [110] has supported the observation of Cu containing atomic column of Q' and C phase configurations.

Some studies [80, 109, 112] have demonstrated that Cu atoms can also be incorporated in β" particles without making the structure disordered. Cu was found to occupy the Si3/Al site in the bulk β" structure [109, 112], as well as in the main β" interface with trace along [230]Al [80]. The latter observation was also made in alloys containing both Li and Cu, see Figure 9. The different observations could be due to difference in size of the observed β" precipitates and different heat treatments. In any case, the Si3/Al site seems to be the most favorable for Cu incorporation in β", which is also supported by DFT calculations [80]. It has been reported [112] that Cu atomic columns were also found at Mg1 sites in precipitates having a small β" cross section.

4.3. Zinc (Zn)

Zn is the main alloying element in Al-Zn-Mg(-Cu) alloys (categorized as 7xxx series aluminum alloys) forming different types of metastable plate-shaped precipitates, called η' phases with {111}Al habit planes. Since Zn generally has a high solubility in aluminum, some interactions of Zn with Mg and Si can be expected during precipitation in Al-Mg-Si alloys. Several studies [113-115] investigated the effect of Zn on precipitates in Al-Mg-Si alloys. No plate-like precipitates on {111}Al planes were observed up to 1 wt% Zn additions in a lean 6060 Al-Mg-Si alloy [113] and not even for 3 wt% Zn addition in a Cu containing Al-Mg-Si alloy [114]. The observed precipitates were pre-β", β", disordered and L phases along <001>Al, demonstrating a preponderance of Si as nucleation agent compared to Zn. However, coexistence of both β" and η precipitates has been observed in a Zn added (3 wt%) Mg-rich Al-Mg-Si alloy [115]. The reason for the different observations in the 3 wt% Zn addition [114, 115] is unknown. These experiments could imply that Cu will prevent nucleation and precipitation of η' phase.

For Zn additions (up to 1 wt%) to Al-Mg-Si alloys, there is no report showing formation of new precipitate types. However, adding Zn makes precipitates disordered [113]. The disordered structures are based on the Si-network commonly known in the Al-Mg-Si(-Cu) system. Zn containing atomic columns are identified both *in-between* and *on* the Si-network columns, see Figure 10. In this respect, the Zn distribution resembles that of Cu in similarly disordered precipitates. However, Zn seems to have less preference for particular atomic sites. For example, it was observed that Zn has a weak preference for the Ag and Al sites in the β'_{Ag} phase [111], see section 4.5. Apart from the disordered precipitates, perfect β" precipitates were also observed in a Zn containing Al-Mg-Si alloy [113]. Here, Zn has only been observed at the Si3/Al site, see Figure 11, and explained in a detailed study [81].

4.4. Germanium (Ge)

Several studies indicate that Ge causes large alterations to the precipitate structures when added to Al-Mg-Si alloys. Ge generally refines the precipitation, leading to an increase in precipitate number density, a decrease in precipitate size and length and consequently increased hardness after heat treatment [37, 116, 117]. A typical feature observed in precipitate cross sections by HAADF-STEM is a projected hexagonal network of high intensity Ge/Si columns, see Figure 12.

Small Ge additions up to ~ 0.1 wt% only partly changes the precipitation sequence of Al-Mg-Si alloys, but often leads to disorder in the β" phase. Similar to the effects of adding Li to Al-Mg-Si alloys, as discussed in section 4.1, Ge tends to alter the stacking of β"-eyes. The β_2" and β_3" stacking variations occur with a much higher frequency than what is observed in alloys with no Ge additions [37], see overview of the three β" variants in Table 3 and Figure 13. These experimental observations have been supported by DFT calculations, suggesting that all three β" configurations are energetically favorable, but more so when Ge replaces Si sites. Based on these findings, the current hypothesis is that β" stacking variations occur early

in the precipitation sequence, while the hexagonal Ge-network is the stable configuration often found after over-aging or in samples with a higher Ge content.

For over-aged alloys or alloys with higher amount of added Ge, Ge causes the Si network to line up along <100>Al instead of <510>Al. By fully replacing Si with Ge, the well-known β" phase is no longer observed, and small "disordered" precipitate structures with the hexagonal Ge-network dominate at peak hardness [116]. Upon over-aging, a majority of the observed precipitates are coherent β'-Ge [118], and quantitative HAADF-STEM suggested the nominal Ge columns in contain about 30% Al or 20% vacancies.

Figure 14 illustrates β_2" and β_3" observed in two different cross sections. The β_2" unit cell has 22 atoms, see Figure 14 (a). The corresponding Al super cell consists of 24 atomic columns, meaning that β_2" can be described as having shed two atomic columns, which it can only do by having absorbed the same amount of vacancies [37]. Although both β" and β_2" are classified as space group C2/m, the c-axis of β_2" lies along the <100>Al, while the c-axis of β" lies along <130>Al. The unit cell of the third stacking variation of β"-eyes, β_3", consists of 26 atomic columns, see Figures 13(c) and 14(b). Here, the c-axis of the unit cell lies along the <-5-10>Al direction. Comparing β_3" to the two other stacking variations, it becomes clear that the deviation lies in the additional Al columns, see Figure 13(c). Observations from HAADF-STEM confirm that all three stacking variations can occur in the same cross section as different fragments, but it seems more probable for β_2" and β_3" to form in cross-section fragments with a higher occupancy of Ge [37].

Revisiting the DFT calculation results given in Figure 3, Ge should be more attractive to Mg atoms as nearest neighbors than Si. It is also more favorable for a vacancy to be in the vicinity of Ge than Si, something that should be positive for increasing the amount of sites for nucleation. These results are supported experimentally as we observe higher precipitate number densities in Ge-added alloys.

4.5. Silver (Ag)

Small additions of Ag have been observed to stimulate GP-zone formation in Mg-containing aluminum alloys and accelerate their age hardening response [119]. Binary Al-Mg alloys, with less than 10 wt% Mg, are considered non-heat-treatable. However, after adding a small amount of Ag, an unmistakable hardening response occurs [119]. This effect is supported by the DFT results in Figure 3, demonstrating that it is energetically favorable for Ag and Mg to be nearest neighbors. This is a prerequisite for forming favorable sites for nucleation of hardening phases, and an analogue to the Mg-Si pair.

Numerous studies of Al-Mg-Si alloys with Ag additions have demonstrated that the Al matrix adjacent to the precipitate-Al interface is Ag-enriched [37, 111, 120]. This effect is clearly illustrated in the HAADF-STEM images in Figure 15 (b), where a high atomic number contrast is detected at the interface of the precipitate cross sections. A cross section growing into the image-plane is illustrated in Figure 15 (c), also exhibiting high Z-contrast at the precipitate-matrix interface.

The first precipitates to form in binary Al-Ag alloys are γ' platelets, growing on {100}Al planes [120] with the familiar Ag-enrichment at the precipitate-Al interface. The precipitate growth is believed to be due to interface control, that is, the γ' plate growth is not just controlled by the availability of solute. This effect is probably due to the challenge of overcoming the energy barrier needed to nucleate additional precipitate ledges [120].

Ag-vacancy complexes are likely to attract other alloying elements and vacancies, making them beneficial sites for nucleation of hardening phases. Figure 3 shows DFT calculations which corroborate such assertions, as the interaction energy between Ag and vacancies is below -0.08 eV. In comparison to Si, which is also known to take part in the nucleation stage, Ag should have an even higher affinity to vacancies.

The cross section in Figure 15(c) incorporates β'_{Ag}, in addition to a significant Ag enrichment of the Al-precipitate interface. As can be observed in Figure 15 (c), β'_{Ag}

(indicated by yellow dashed lines) has a hexagonal symmetry. However, as compared to β', the cell dimensions shrink from 0.72 nm to 0.69 nm [111], see black arrows in the enlarged square in Figure 15 (c). The dimensions of the unit cell are given in Table 4. Ag replaces one of the three Si-network atomic columns in the unit cell, this replacement can be done partially or fully. However, the replacement does not seem to cause any noteworthy effect on the periodicity of the projected Si-network, which appears to be continuous across the different domain boundaries of the precipitate [111, 121].

The investigations performed by Marioara et al. [111] further justified Ag-incorporated U2 phases [111]. The intensities of Al atomic columns were systematically higher than those of Si, indicating the presence of Ag. All the precipitate structures which were analyzed in the study by Marioara et al. [111] were complex and contained ordered domains, separated by a high number of anti-phase boundaries. HAADF-STEM investigations suggested that the U2 phase was altered by partly substituting Al by Ag. This resulted in a $U2_{Ag}$ phase with an expanded unit cell compared to U2, allowing the phase connection to be fully coherent.

In addition to the above mentioned behavior, Ag occupies particular sites in the precipitate crystal structures. By combining EELS and HAADF-STEM it has been demonstrated that Ag can substitute atoms in atomic columns otherwise known to contain Al [122]. The same work also identified a co-existence of Ag and Si on the hexagonal Si-network. The Mg and Ag signals detected by EELS were not found to coincide at any point [122].

Q' and C phases are, as mentioned in section 4.2, very common in Cu-added Al-Mg-Si alloys. There are however cases where the same phase fragments have occurred in Cu-free alloys, and the phases have been identified to contain Ag instead of Cu [37]. These results illustrate how silver is able to initiate the same phases as Cu does in this alloy system. An example of a cross section incorporating Q'_{Ag} is given in Figure 16(a), with the model of the

phase in Figure 16 (b). DFT calculations have also deemed it energetically favorable for the Q' phase to form when the Cu columns are replaced by Ag [37]. The formation energy does however suggest that it is slightly more favorable for Q' with Cu to form than Q' with Ag, which could be one of the reasons why Q' does indeed contain Cu instead of Ag if both elements are added to the alloy [122].

4.6. Nickel (Ni), cobalt (Co), gold (Au) and other elements

To this point there has not been done any detailed study on the effect of Ni, Co and Au on precipitate atomic structures in the Al-Mg-Si system. These elements have low solid solubility in aluminum in general. However, several observations (Figure 17) can be made with respect to incorporations of these elements in precipitates. No new precipitate types have been observed in Ni, Co or Au containing alloys. However, these elements are found preferentially at the precipitate/matrix interface and either occupy sites *in-between* or *on* the Si network. Experimental conditions for the Ni, Co or Au containing alloys are shown in Appendix B. Some representative examples demonstrating the effects of these elements on precipitate structures are shown in Figure 17 and summarized in the following paragraphs. Further detailed studies are necessary to understand the effect of these elements better.

Ni has a weak influence on the precipitate structures. Ni atoms are found at the interfaces of β” precipitates at peak hardness condition. The Ni atoms are incorporated *on* the Si network sites, and partly make β” disordered around the Ni containing sites. Ni may be described as "destroying the β” eyes", see Figure 17.

Co has a weak influence on the precipitate structures. Co atoms are found at interface of β’ precipitates in over-aged condition. The Co atoms are incorporated *in-between* the Si network sites. In this precipitate, it was observed that the interface is aligned along <100>Al with the Co incorporations, which interestingly is analogue to Cu atoms situated at the interface of the C phase [91].

Au has some influences on precipitate structures. Au atoms are found at the interface of β' precipitates in an over-aged condition. The Au atoms are incorporated *on* the Si network sites.

Additionally, small, spherical particles which enhance the nucleation of hardening precipitates can be formed by adding small amounts of Cd [123] and Sn [124, 125] to any aluminum alloy. Based on these observations [123-125], some influences on precipitate atomic structures may be expected also in the Al-Mg-Si system. To the best of the authors' knowledge, there has been no report and detailed investigations of precipitate atomic structures in such alloy systems containing Cd or Sn.

5. Summary

The effects of the selected elements on precipitate atomic structure have been summarized. Additional elements can have strong effects on the precipitate microstructure in Al-Mg-Si alloys, and can enter various atomic positions in the structures. Solute additions have the ability to change the precipitation sequences or alter ordered phases into disordered structures. In the precipitates Si columns form a network which is hexagonal in projection along the main extension, but which is periodically interrupted in β". The following is a brief summary of the effect of each element on the precipitate atomic structures.

- Lithium (Li)
    - Changes stacking of β" eyes.
    - Li atoms particularly occupy Mg3 sites in the β" phase and DFT calculations suggest Li may occupy Mg1 sites as well.
- Copper (Cu)
    - Changes precipitation sequence of Al-Mg-Si system and makes different precipitate types, most notably C, L and Q' phases.

    - Makes precipitates disordered. Cu atoms occupy sites both *in-between* and *on* the Si-network in the disordered precipitates.
    - Cu atoms occupy the Si3/Al site of the β" phase both at the interface along <320>Al and in the bulk, and at Mg1 site in bulk.
- Zinc (Zn)
    - Forms no new precipitate types with moderate additions.
    - Makes precipitates disordered. Zn atoms occupy sites both *in-between* and *on* the Si-network in disordered precipitates, will less preferred sites as compared to Cu.
    - Zn atoms occupy the Si3/Al site of the β" phase in bulk precipitates.
- Germanium (Ge)
    - Change stacking of β" eyes.
    - Create a projected hexagonal Ge-network.
    - Initiate disordered precipitate phases
    - When fully substituting Si, β'-Ge dominates.
- Silver (Ag)
    - Enriches the precipitate/matrix interface.
    - Makes its own precipitate types: β'_{Ag}.
    - Ag atoms are situated *in-between* the Si network, Q'/C type local atomic configurations.
    - May partly occupy Si atomic columns in bulk.
    - May partly occupy Al atomic columns in bulk.
- Nickel (Ni)
    - Forms no new precipitate types.
    - Make β" precipitate partly disordered in a peak hardness condition. Ni atoms are occupied *on* the Si network.

- Cobalt (Co)
    - Forms no new precipitate types.
    - Found at interface of β’ and aligned along <100>Al in an over-aged condition. Co atoms occupy sites *in-between* the Si network.
- Gold (Au)
    - Forms no new precipitate types.
    - Found at interface of β’ in an over-aged condition. Au atoms occupy sites *on* the Si network.

Accurate information of how additions of elements affect the precipitate microstructure and properties is expected to become of increasing importance for further development and tailoring of properties of alloys. In order to obtain desired macroscopic properties, such as strength, ductility, corrosion, conductivity, toughness, formability, fatigue, creep, high temperature stability and crash performance, better control and understanding of nucleation and growth of the precipitates are required.

As a final remark, it is worth noting that recent observations of precipitates include "beyond 6xxx series", i.e. coexistence of the other precipitate types in an Al matrix by including elements, such as Cu and Zn in higher amounts, and manipulating heat treatment. For example, it has been observed [126] that the coexistence of L, S, θ’, σ, Ω and η phases, i.e. precipitate types of 6xxx, 2xxx and 7xxx series alloys, in the same Al matrix. Such coexistences were also observed by ref. [105] showing Q' (6xxx series) and θ’ (2xxx series) and by ref. [115] showing β’ (6xxx series) and η (7xxx series). These observations imply that alloys could drastically change properties and open up further alloy development for optimization of alloys to a large degree in the future.

Appendix A: Methodologies and structural solutions

All the structural analysis in this paper have been done by transmission electron microscopy (TEM) based techniques. Although other important characterization tools (e.g. atom probe tomography) can be raised for structural analysis, the combination of high angle annular dark field scanning electron microscopy (HAADF-STEM) and density functional theory (DFT) calculations has been a crucial technique to reveal the atomic structures in detail. The following text lists short descriptions of those techniques. Detailed descriptions of the methodologies can be found elsewhere, e.g. refs. [28, 37, 81].

HAADF-STEM techniques

TEM is a technique highly suited to investigate the structure of individual nanometer-sized precipitates. Above all, HAADF-STEM (sometimes coupled with spectroscopic techniques) is the most important technique used for the precipitate structural analysis at the atomic scale.

In STEM a convergent electron beam is focused into a small probe which scans across the specimen. The electrons which are transmitted and scattered through the specimen, or including the signals resulting from specimen-electron beam interactions, are detected, see Figure 18. In particular, high angle incoherently scattered electrons are detected by an HAADF detector. Electrons experiencing Rutherford scattering or thermal diffuse scattering are scattered to high angles, dependent on their atomic number (Z), which is why HAADF-STEM images have atomic number contrast. That is, high Z elements will correspond to higher intensity in the images [127, 128].

Aberration correction [129, 130] of the probe forming lens in a STEM setup has made it possible to obtain HAADF-STEM images with atomic scale resolution. Figure 19 shows the comparison of conventional high resolution TEM (phase contrast), aberration uncorrected HAADF-STEM and corrected HAADF-STEM for a Q' precipitate.

Density Functional Theory (DFT)

Density functional theory (DFT) is based on the standard theory of quantum mechanical systems, and is becoming increasingly important for the simulation of electronic properties of atoms, molecules and condensed phases.

The main application of DFT is to determine three-dimensional electron structure in a many-body system. The theoretical framework for DFT is based on the two theorems of Hohenberg-Kohn [132]. The first theorem states that for a system in its ground state, the electron density can be used to determine the external potentials acting on the electrons. The second theorem states that the energy of an electronic system is a unique functional of the electron density. The density that minimizes the energy is the ground state energy. Based on these theorems, Kohn and Sham developed a practical method for reducing the many-body problem spatial coordinates to the electron density functional, depending only on 3 spatial coordinates [133].

The Kohn Sham equations are the time-independent Schrdinger equations (one for each electron), and they can be expressed as:

$$\left(-\frac{\hbar^2}{2m}\nabla^2 + \upsilon_{effective}(\vec{r})\right)\phi_i(\vec{r}) = \epsilon_i\phi_i(\vec{r}) \qquad (3)$$

In (3) $\hbar$ is the reduced Planck constant, h divided by 2π. The effective potential at position (r) is $\upsilon_{effective}$, the orbital energy is ϵ_i and the Kohn-Sham orbital is $\phi_i(\vec{r})$. The electron density, $\rho(\vec{r})$ on an N-body system is here given as:

$$\rho(\vec{r}) = \sum_i^N |\phi_i(\vec{r})|^2 \qquad (4)$$

$v_{effective}(\vec{r})$ is a function of the electron density, the external nuclei potentials and the exchange correlation potential.

$$v_{effective}(\vec{r}) = v_{external}(\vec{r})e^2 + \int \frac{\rho(\vec{r})}{\vec{r}-\vec{r'}} d\vec{r} + v_{ex-corr}[\rho] \quad (5)$$

The total energy of the system, $E[\rho]$, can be expressed as:

$$E[\rho] = T_s[\rho] + \int v_{external}(\vec{r})\,\rho(\vec{r}) d\vec{r} + V_H + E_{ex-corr}[\rho] \quad (6)$$

Where T_s is the kinetic energy, V_H is the Coulomb potential and $E_{ex-corr}$ is the exchange-correlation energy.

Interaction Energies

When applying DFT to calculate the bonding energies between solute elements it is common to base the lattice parameter on the relaxation of an aluminum supercell. Interaction energies can then be estimated from the difference between the total energies. All calculations should have the same cell size and parameter settings so that systematic errors cancel out.

The interaction energies presented in this paper are based on DFT calculations using the Vienna ab initio simulation package (VASP), using the projector augmented wave method (PAW) within the Perdew-Burke-Ernzehof (PBE) generalized gradient approximation. Separate calculations performed by the tetrahedron method with Blchl correction for smearing was used for accurate energies.

Assuming an aluminum supercell consisting of 5x5x5 aluminum unit cells, the interaction energies can be calculated based on Equation 7 and Equation 8.

$$E_Y = E_{Al499Y} - \frac{499}{500} E_{Al500} \quad (7)$$

$$E_{YZ} = E_{Al498YZ} - \frac{498}{500} E_{Al500} - E_Y - E_Z \quad (8)$$

Y and Z represents an atom or a vacancy which is replacing an Al atom in the cell. The solid solution energies of atoms Y and Z are denoted E_Y and E_Z respectively.

Appendix B: Experimental details for previously unpublished results

Experimental procedures of the observations of Ni, Co or Au containing precipitates shown in section 4.6 are described in the following.

Al-1.0wt%Mg2Si having 0.1 wt% Ni, 0.1wt% Co or 0.01wt% Au were used for the experiment. The alloys were cast and subsequently homogenized at 540°C for 4 days. The samples were further solution heat treated at 575°C for 6 hours, and subsequently water quenched. They were further artificially aged at 200°C for 200 min and 4000 min for the Au containing alloy and for the Ni and Co containing alloys, respectively.

HAADF-STEMspecimens were prepared by electropolishing using a Tenupol 5 machine (Struers). The electrolyte consisted of 1/3 vol.% HNO3 in methanol and the solution was kept at a temperature between -20 and -35°C. Thickness of the HAADF-STEM specimens were about 50-80 nm.

HAADF-STEM images were taken by a spherical aberration (C_S) probe corrected JEOL ARM 200F with cold field emission operated at 200 kV. The inner and outer collection angles of the HAADF detector were in the range of 45 - 150 mrad and the probe size was 0.1 nm. In order to reduce contamination on the specimen during taking HAADF-STEM images, all the specimens were cleaned in plasma cleaner (Fishione) before the imaging. Fast Fourier

transform (FFT) filtering has been applied to the HAADF-STEM images in order to reduce noise using a circular band pass mask which removes all period shorter than 0.15 nm.

Received: ((will be filled in by the editorial staff))
Revised: ((will be filled in by the editorial staff))
Published online: ((will be filled in by the editorial staff))

[1] I. Polmear, *Materials Forum*, **2004**, *28*, 1-14.

[2] G. A. Edwards, K. Stiller, G. L. Dunlop, M. J. Couper, *Mater. Sci. Forum*, **1999**, *217-222*, 713-718.

[3] M. Murayama, K. Hono, *Acta Mater.*, **1999**, *47*, 1537-1548.

[4] K. Matsuda, Y. Sakaguchi, Y. Miyata, Y. Uetani, T. Sato, A. Kamio, S. Ikeno, *J. Mater. Sci.*, **2000**, *35*, 179-189.

[5] S. Ringer, K. Hono, *Materials Characterization*, **2000**, *44* 101-131.

[6] O. Myhr, Ø. Grong, S. Andersen, *Acta Materialia*, **2001**, *49*, 65-75.

[7] S. Esmaeili, X. Wang, D. J. Lloyd, W. J. Poole, *Metallurgical and Materials Transactions A*, **2003**, *34*, 751-763.

[8] X. Wang, J. D. Embury, W. J. Poole, S. Esmaeili, D. J. Lloyd, *Metallurgical and Materials Transactions A*, **2003**, *34*, 2913-2924.

[9] F. De Geuser, W. Lefebvre, D. Blavette, *Phil. Mag. Lett.*, **2006**, *86*, 227-234.

[10] A. Serizawa, S. Hirosawa, T. Sato, *Mater. Trans. A*, **2008**, *39*, 243-251.

[11] C. D. Marioara, S. J. Andersen, J. Jansen, H. W. Zandbergen, *Acta Materialia*, **2003**, *51*, 789-796.

[12] C. D. Marioara, S. J. Andersen, H. Zandbergen, R. Holmestad, *Metallurgical and Materials Transactions A*, **2005**, *36*, 691-702.

[13] M. Torsæter, H. S. Hasting, W. Lefebvre, C. D. Marioara, J. C. Walmsley, S. J. Andersen, R. Holmestad, *J. Appl. Phys.*, **2010**, *108*, 073527.

[14] J. Banhart, C. S. T. Chang, Z. Liang, N. Wanderka, M. D. H. Lay, A. J. Hill, *Adv. Eng. Mater.*, **2010**, *12*, 559-571.

[15] J. Banhart, M. D. H. Lay, C. S. T. Chang, A. J. Hill, *Phys. Rev. B*, **2011**, *83*, 014101.

[16] S. Pogatscher, H. Antrekowitsch, H. Leitner, T. Ebner, P. Uggowitzer, *Acta Mater.*, **2011**, *59*, 3352-3363.

[17] M. Starink, L. Cao, P. Rometsch, *Acta Mater.*, **2012**, *60*, 4194-4207.

[18] R. Marceau, A. de Vaucorbeil, G. Sha, S. Ringer, W. Poole, *Acta Mater.*, **2013**, *61*, 7285-7303.

[19] S. Pogatscher, H. Antrekowitsch, H. Leitner, A. Sologubenko, P. Uggowitzer, *Scripta Mater.*, **2013**, *68*, 158-161.

[20] M. Zandbergen, Q. Xu, A. Cerezo, G. Smith, *Acta Mater.*, **2015**, *101*, 136-148.

[21] M. Zandbergen, A. Cerezo, G. Smith, *Acta Mater.*, **2015**, *101*, 149-158.

[22] S. J. Andersen, H. W. Zandbergen, J. Jansen, C. Træholt, U. Tundal, O. Reiso, *Acta Mater.*, **1998**, *46*, 3283-3298.

[23] C. Wolverton, *Acta Mater.*, **2001**, *49*, 3129-3142.

[24] C. D. Marioara, S. J. Andersen, J. Jansen, H. W. Zandbergen, *Acta Mater.*, **2001**, *49*, 321-328.

[25] C. Ravi, C. Wolverton, *Acta Mater.*, **2004**, *52*, 4213-4227.

[26] M. van Huis, J. Chen, H. Zandbergen, M. Sluiter, *Acta Mater.*, **2006**, *54*, 2945-2955.

[27] H. S. Hasting, A. G. Frseth, S. J. Andersen, R. Vissers, J. C.Walmsley, C. D. Marioara, F. Danoix, W. Lefebvre, R. Holmestad, *J. Appl. Phys.*, **2009**, *106*, 123527.

[28] P. H. Ninive, A. Strandlie, S. Gulbrandsen-Dahl, W. Lefebvre, C. D. Marioara, S. J. Andersen, J. Friis, R. Holmestad, O. M. Løvvik, *Acta Mater.*, **2014**, *69*, 126-134.

[29] F. J. H. Ehlers, S. Wenner, S. J. Andersen, C. D. Marioara, W. Lefebvre, C. B. Boothroyd, R. Holmestad, *J. Mater. Sci.*, **2014**, *49*, 6413-6426.

[30] M. Dumont, W. Lefebvre, B. Doisneau-Cottignies, A. Deschamps, *Acta Mater.*, **2005**, *53*, 2881-2892.

[31] L. Kovarik, P. Gouma, C. Kisielowski, S. Court, M. Mills, *Acta Mater.*, **2004**, *52*, 2509-2520.

[32] L. A. Westfall, Queens University, Kingston, volume 1, Ontario, Canada.

[33] V. Gavini, K. Bhattacharya, M. Ortiz, *Phys. Rev. B*, **2007**, *76*, 180101.

[34] D. Simonovic, M. H. F. Sluiter, *Phys. Rev. B*, **2009**, *79*, 054304.

[35] S. Hirosawa, F. Nakamura, T. Sato, *Mater. Sci. Forum*, **2007**, *561-565*, 283-286.

[36] S. Hirosawa, F. Nakamura, T. Sato, T. Hoshino, *J. J. Inst. Light Metals*, **2006**, *56*, 621-628.

[37] E. A. Mørtsell, S. J. Andersen, J. Friis, C. D. Marioara, R. Holmestad, *Philos. Mag.*, **2017**, *97*, 851-866.

[38] E. A. Mørtsell, Ph.D. thesis, Norwegian University of Science and Technology (NTNU), **2016**.

[39] Y. L. Liu, S. B. Kang, *J. Mater. Sci.*, **1997**, *32*, 1443-1447.

[40] Y. Liu, S. Kang, H. Kim, *Mater. Lett.*, **1999**, *41*, 267-272.

[41] N. Kuijpers, F. Vermolen, C. Vuik, P. Koenis, K. Nilsen, S. van der Zwaag, *Mater. Sci. Eng. A*, **2005**, *394*, 9-19.

[42] S. Zajac, B. Hutchinson, A. Johansson, L.-O. Gullman, *Mater. Sci. Technol.*, **1994**, *10*, 323-333.

[43] F. Humphreys, M. Hatherly, in second edition, (Eds: F. Humphreys, M. Hatherly), Elsevier, **2004**, Ch.15.

[44] H.Westengen, L. Auran, O. Reiso, *Aluminium*, **1981**, *57*, 797-803.

[45] L. Lodgaard, N. Ryum, *Mater. Sci. Eng. A*, **2000**, *283*, 144-152.

[46] E. Nes, H. Billdal, *Acta Metall.*, **1977**, *25*, 1039-1046.

[47] J. Robson, P. Prangnell, *Acta Mater.*, **2001**, *49*, 599-613.

[48] O. Reiso, H. Westengen, L. Auran, 7th International Light Metals Congress Leoben/Vienna, 186-188.

[49] J. Røyset, N. Ryum, *Mater. Rev.*, **2005**, *50*, 19-44.

[50] Y. Bekki, K. Koyama, Y. Himuro, *Mater. Sci. Forum*, **2006**, *396*, 501-506.

[51] H. Hallem, B. Forbord, K. Marthinsen, *Mater. Sci. Eng. A*, **2004**, *387*, 940-943.

[52] Z.-H. Jia, H.-L. Huang, X.-L. Wang, Y. Xing, Q. Liu, *Acta Metall. Sin.*, **2016**, *29*, 105-119.

[53] M. J. Starink, P. J. Gregson, P. Rometsch, A. Harriss, S. C. Wang, *Mater. Sci. Forum*, **2002**, *396*, 655-660.

[54] D. Bratland, . Grong, H. Shercli, O. Myhr, S. Tjøtta, *Acta Mater*. **1997**, *45*, 1-22.

[55] K. Strobel, M. A. Easton, L. Sweet, M. J. Couper, J.-F. Nie, *Mater. Trans.*, **2011**, *52*, 914-919.

[56] K. Matsuda, K. Kido, S. Taniguchi, Y. Uetani, S. Ikeno, *J. J. Inst. Light Metals*, **2002**, *52*, 398-402.

[57] S. Wang, K. Matsuda, T. Kawabata, Y. Zou, T. Yamazaki, S. Ikeno, *Mater. Trans.*, **2011**, *52*, 229-234.

[58] Z. Fan, Y. Wang, Y. Zhang, T. Qin, X. Zhou, G. Thompson, T. Pennycook, T.Hashimoto, *Acta Mater.*, **2015**, *84*, 292-304.

[59] F. Wang, Z. Liu, D. Qiu, J. A. Taylor, M. A. Easton, M.-X. Zhang, *Acta Mater.*, **2013**, *61*, 360-370.

[60] Y. Du, Y. Chang, B. Huang, W. Gong, Z. Jin, H. Xu, Z. Yuan, Y. Liu, Y. He, F.-Y. Xie, *Mater. Sci. Eng. A*, **2003**, *363*, 140-151.

[61] M. Mantina, Y. Wang, L. Chen, Z. Liu, C. Wolverton, *Acta Mater.*, **2009**, *57*, 4102-4108.

[62] S. Andersen, C. Marioara, R. Vissers, A. Frøseth, H. Zandbergen, *Mater. Sci. Eng. A*, **2007**, *444*, 157-169.

[63] S. Wenner, C. D. Marioara, S. J. Andersen, R. Holmestad, *Mater. Sci. Eng. A*, **2013**, *575*, 241-247.

[64] X. Wang, H. Huang, X. Gu, Y. Li, Z. Jia, Q. Liu, *J. Appl. Cryst.*, **2016**, *49*, 1223-1230.

[65] J. Zhang, Z. Fan, Y. Wang, B. Zhou, *Mater. Sci. and Technol.*, **2001**, *17*, 494-496.

[66] H. W. Zandbergen, S. J. Andersen, J. Jansen, *Science*, **1997**, *277*, 1221-1225.

[67] C. Cayron, P. A. Buffat, *Acta Mater.*, **2000**, *48*, 2639-2653.

[68] R. Vissers, M. A. van Huis, J. Jansen, H. W. Zandbergen, C. D. Marioara, S. J. Andersen, *Acta Mater.*, **2007**, *55*, 3815-3823.

[69] S. J. Andersen, C. D. Marioara, A. Frseth, R. Vissers, H. W. Zandbergen, *Mater. Sci. Eng. A*, **2005**, *390*, 127-138.

[70] R. Vissers, C. D. Marioara, S. J. Andersen, R. Holmestad, *Proceedings of ICAA11, volume Vol. 2*, 1263-1269.

[71] N. A. Bul'enkov, A. G. Yakovenko, O. M. Ul'yanikhina, *J. Struct. Chemist.*, **1971**, *11*, 1059-1061.

[72] M. H. Jacobs, *Phil. Mag.*, **1972**, *26*, 1-13.

[73] C. D. Marioara, S. J. Andersen, A. Birkeland, R. Holmestad, *J. Mater. Sci.*, **2008**, *43*, 4962-4971.

[74] K. Matsuda, S. Tada, S. Ikeno, T. Sato, A. Kamio, *Scripta Metall. Mater.*, **1995**, *32*, 1175-1180.

[75] G. Edwards, K. Stiller, G. Dunlop, M. Couper, *Acta Mater.*, **1998**, *46*, 3893-3904.

[76] G. Sha, H. Mller, W. Stumpf, J. Xia, G. Govender, S. Ringer, *Acta Mater.*, **2012**, *60*, 692-701.

[77] F. J. Ehlers, *Comput. Mater. Sci.*, **2014**, *81*, 617-629.

[78] S. Wenner, L. Jones, C. D. Marioara, R. Holmestad, *Micron*, **2017**, *96* 103-111.

[79] J. H. Chen, E. Costan, M. A. van Huis, Q. Xu, H. W. Zandbergen, *Science*, **2006**, *312*, 416-419.

[80] T. Saito, F. J. Ehlers, W. Lefebvre, D. Hernandez-Maldonado, R. Bjørge, C. D. Marioara, S. J. Andersen, E. A. Mørtsell, R. Holmestad, *Scripta Mater.*, **2016**, *110*, 6-9.

[81] T. Saito, F. J. Ehlers, W. Lefebvre, D. Hernandez-Maldonado, R. Børge, C. D. Marioara, S. J. Andersen, R. Holmestad, *Acta Mater.*, **2014**, *78*, 245-253.

[82] E. A. Mørtsell, C. D. Marioara, S. J. Andersen, I. G. Ringdalen, J. Friis, S. Wenner, J. Røyset, O. Reiso, R. Holmestad, *J. Alloys Compd.*, **2017**, *699*, 235-242.

[83] W. Yang, M. Wang, R. Zhang, Q. Zhang, X. Sheng", *Scripta Mater.*, **2010**, *62*, 705-708.

[84] S. J. Andersen, C. D. Marioara, R. Vissers, A. Frøseth, P. M. Derlet, *13th European Microscopy Congress (EMC 2004)*, volume 2, 599.

[85] S. J. Andersen, C. D. Marioara, J. Friis, R. Bjørge, Q. Du, I. Ringdalen, S. Wenner, E. A. Mørtsell, R. Holmestad, T. Saito, J. Røyset, O. Reiso, *Mater. Sci. Forum*, **2017**, *877*, 461-470.

[86] I. J. Polmear, *Light Alloys*, Elsevier, **2006**.

[87] Y. Koshino, M. Kozuka, S. Hirosawa, Y. Aruga, J. Alloys Compd., 2015, 622, 765-770.

[88] S. P. Cooil, E. A. Mørtsell, F. Mazzola, M. Jorge, S. Wenner, M. T. Edmonds, L. Thomsen, H. W. Klemm, G. Peschel, A. Fuhrich, M. Prieto, T. Schmidt, J. A. Miwa, R. Holmestad, J. W. Wells, *Materials Research Express*, **2016**, *1005*, 116501.

[89] D. Chakrabarti, D. E. Laughlin, *Progress in Materials Science*, **2004**, *49*, 389-410.

[90] C. D. Marioara, S. J. Andersen, T. N. Stene, H. Hasting, J. Walmsley, A. T. J. Van Helvoort, R. Holmestad, *Phil. Mag.*, **2007**, *87*, 3385-3413.

[91] M. Torsæter, F. J. H. Ehlers, C. D. Marioara, S. J. Andersen, R. Holmestad, *Phil. Mag.*, **2012**, *92*, 3833-3856.

[92] C. Cayron, L. Sagalowicz, O. Beffort, P. A. Buffat, *Phil. Mag. A*, **1999**, *79*, 2833-2851.

[93] K. Matsuda, S. Ikeno, Y. Uetani, T. Sato, Metall. *Mater. Trans. A*, **2001**, *32*, 1293-1299.

[94] L. Arnberg, B. Aurivillius, *Acta Chem. Scand.*, **1980**, *34A*, 1-5.

[95] M. Torsæter, W. Lefebvre, C. D. Marioara, S. J. Andersen, J. C.Walmsley, R. Holmestad, *Scripta Mater.*, **2011**, *64*, 817-820.

[96] C. D. Marioara, S. J. Andersen, J. Røyset, O. Reiso, S. Gulbrandsen-Dahl, T.-E. Nicolaisen, I.-E. Opheim, J. F. Helgaker, R. Holmestad, *Metal. and Mater. Trans. A*, **2014**, *45*, 2938-2949.

[97] K. Buchanan, K. Colas, J. Ribis, A. Lopez, J. Garnier, *Acta Mater.*, **2017**, *132*, 209-221.

[98] Z. Jia, L. Ding, L. Cao, R. Sanders, S. Li, Q. Liu, *Metall. Mater. Trans. A*, **2017**, *48*, 459-473.

[99] W. Yang, M. Wang, X. Sheng, Q. Zhang, L. Huang, *Phil. Mag. Lett.*, **2011**, *91*, 150-160.

[100] L. Ding, Z. Jia, Y. Weng, Y. Liu, S. Wu, Q. Liu, *Materials Charact.*, **2016**, *118*, 279-283.

[101] K. Matsuda, D. Teguri, Y. Uetani, T. Sato, S. Ikeno, *Scripta Mater.*, **2002**, *47*, 833-837.

[102] G. Phragmen, *J. Inst. Metals*, **1950**, *77*, 489-552.

[103] A. Biswas, D. J. Siegel, D. N. Seidman, *Acta Mater.*, **2014**, *75*, 322-336.

[104] A. Bobel, K. Kim, C. Wolverton, M. Walker, G. B. Olson, *Acta Mater.*, **2017**, *138*, 150-160.

[105] Q. Xiao, H. Liu, D. Yi, D. Yin, Y. Chen, Y. Zhang, B. Wang, *J. Alloys Compd.*, **2017**, *695*, 1005-1013.

[106] T. Saito, S. Muraishi, C. D. Marioara, S. J. Andersen, J. Røyset, R. Holmestad, *Metall. Mater. Trans. A*, **2013**, *44*, 4124-4135.

[107] T. Saito, C. D. Marioara, J. Ryset, K. Marthinsen, R. Holmestad, *Mater. Sci. Eng. A*, **2014**, *609*, 72-79.

[108] T. Saito, C. D. Marioara, S. J. Andersen, W. Lefebvre, R. Holmestad, *Phil. Mag.*, **2014**, *94*, 520-531.

[109] L. Ding, Z. Jia, J.-F. Nie, Y. Weng, L. Cao, H. Chen, X. Wu, Q. Liu, *Acta Mater.*, **2018**, *145*, 437-450.

[110] L. Ding, H. Hu, Z. Jia, Y. Weng, X. Wu, Q. Liu, *Scripta Mater.*, **2016**, *118*, 55-59.

[111] C. D. Marioara, J. Nakamura, K. Matsuda, S. J. Andersen, R. Holmestad, T. Sato, T. Kawabata, S. Ikeno, *Phil. Mag.*, **2012**, *92*, 1149-1158.

[112] K. Li, A. Bch, M. Song, G. Sha, X. Lu, K. Zhang, Y. Du, S. P. Ringer, D. Schryvers, *Scripta Mater.*, **2014**, *75*, 86-89.

[113] T. Saito, S. Wenner, E. Osmundsen, C. D. Marioara, S. J. Andersen, J. Røyset, W. Lefebvre, R. Holmestad, *Phil. Mag.*, **2014**, *94*, 2410-2425.

[114] M. X. Guo, X. K. Zhang, J. S. Zhang, L. Z. Zhuang, *J. Mater. Sci.*, **2017**, *52*, 1390-1404.

[115] X. Ding, H. Cui, J. Zhang, H. Li, M. Guo, Z. Lin, L. Zhuang, J. Zhang, *Materials & Design*, **2015**, *65*, 1229-1235.

[116] R. Bjørge, C. D. Marioara, S. J. Andersen, R. Holmestad, *Metall. Mater. Trans. A*, **2010**, *41*, 1907-1916.

[117] E. A. Mørtsell, C. D. Marioara, S. J. Andersen, J. Røyset, O. Reiso, R. Holmestad, *Metall. Mater. Trans. A*, **2015**, *46*, 4369-4379.

[118] R. Bjørge, C. Dwyer, M.Weyland, P. Nakashima, C.Marioara, S. Andersen, J. Etheridge, R. Holmestad, *Acta Mater.*, **2012**, *60*, 3239-3246.

[119] M. Kubota, J. F. Nie, B. C. Muddle, *Mater. Trans.*, **2004**, *45*, 3256-3263.

[120] J. M. Rosalie, C. Dwyer, L. Bourgeois, *Acta Mater.*, **2014**, 69, 224-235.

[121] J. Nakamura, K. Matsuda, T. Kawabata, T. Sato, Y. Nakamura, S. Ikeno, *Mater. Trans.*, **2010**, *51*, 310-316.

[122] E. A. Mørtsell, S. Wenner, P. Longo, S. J. Andersen, C. D. Marioara, R. Holmestad, *Micron*, **2016**, *86*, 22-29.

[123] B. Noble, *Acta Metall.*, **1968**, *16*, 393-401.

[124] I. Poon, R. Marceau, J. Xia, X. Liao, S. Ringer, *Mater. Design*, **2016**, *96*, 385-391.

[125] L. Bourgeois, J. F. Nie, B. C. Muddle, *Mater. Sci. Forum*, **2002**, *396*, 789-794.

[126] S. Wenner, C. D. Marioara, S. J. Andersen, M. Ervik, R. Holmestad, *Mater. Charact.*, **2015**, *106*, 226-231.

[127] T. Yamazaki, M. Kawasaki, K. Watanabe, I. Hashimoto, M. Shiojiri, *Ultramicroscopy*, **2002**, *92*, 181-189.

[128] P. Nellist, S. Pennycook, *Ultramicroscopy*, **1999**, *78*, 111-124.

[129] O. Krivanek, N. Dellby, A. Lupini, *Ultramicroscopy*, **1999**, *78*, 1-11.

[130] P. E. Batson, N. Dellby, O. L. Krivanek, *Nature*, **2002**, *418*, 617-620.

[131] T. Saito, Ph.D. thesis, Norwegian University of Science and Technology (NTNU), **2014**.

[132] P. Hohenberg, W. Kohn, *Phys. Rev.*, **1964**, *136*, B864-B871.

[133] W. Kohn, L. J. Sham, *Phys. Rev.*, **1965**, *140*, A1133-A1138.

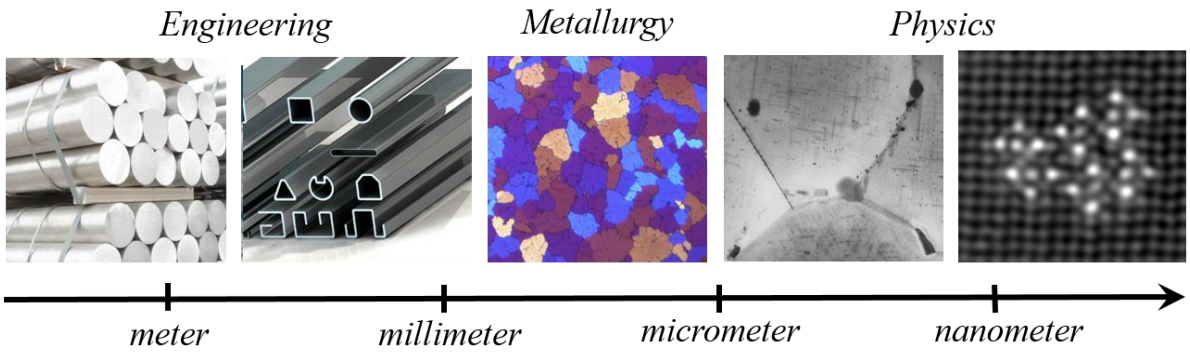

Figure 1: Zooming down from the macro-scale to the atomic scale – going from engineering field via metallurgy to the physics field.

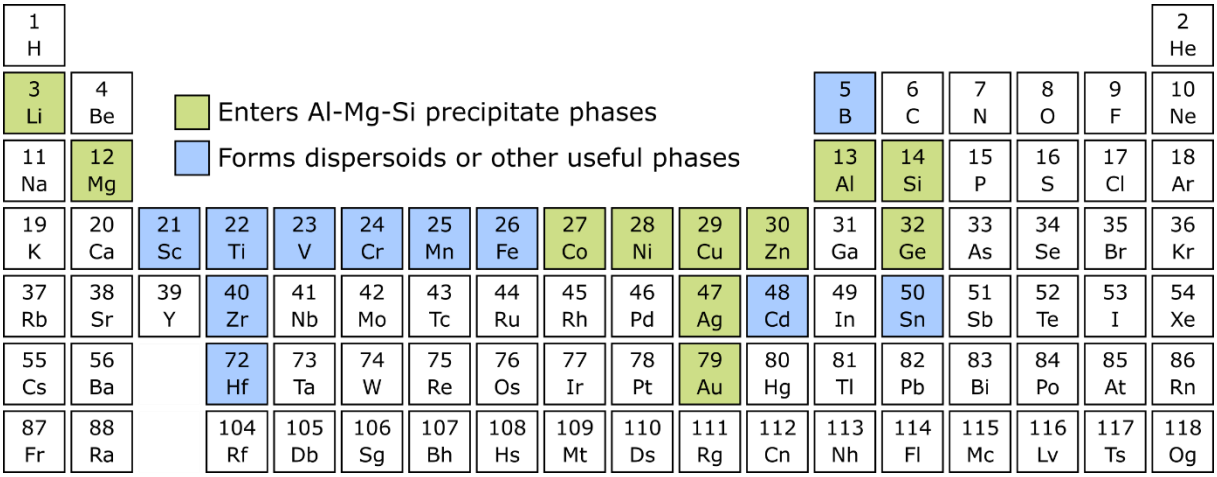

Figure 2: The periodic table of elements, highlighting the elements mentioned in this paper and categorizing their effect in Al-Mg-Si alloys.

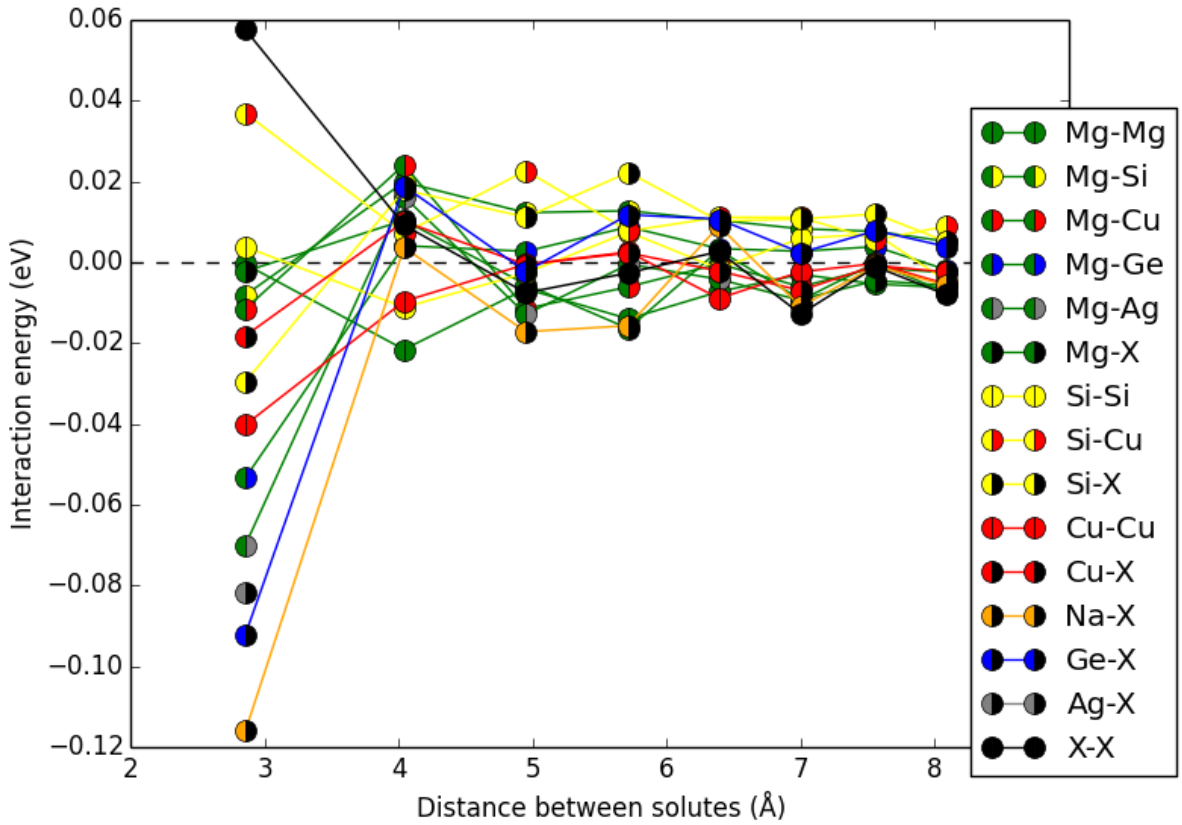

Figure 3: Interaction energies between the alloying elements and/or vacancies (X) in fcc aluminum as a function of separation distance, from 1st to 8th nearest neighbors. Reproduced with permission from ref. [38].

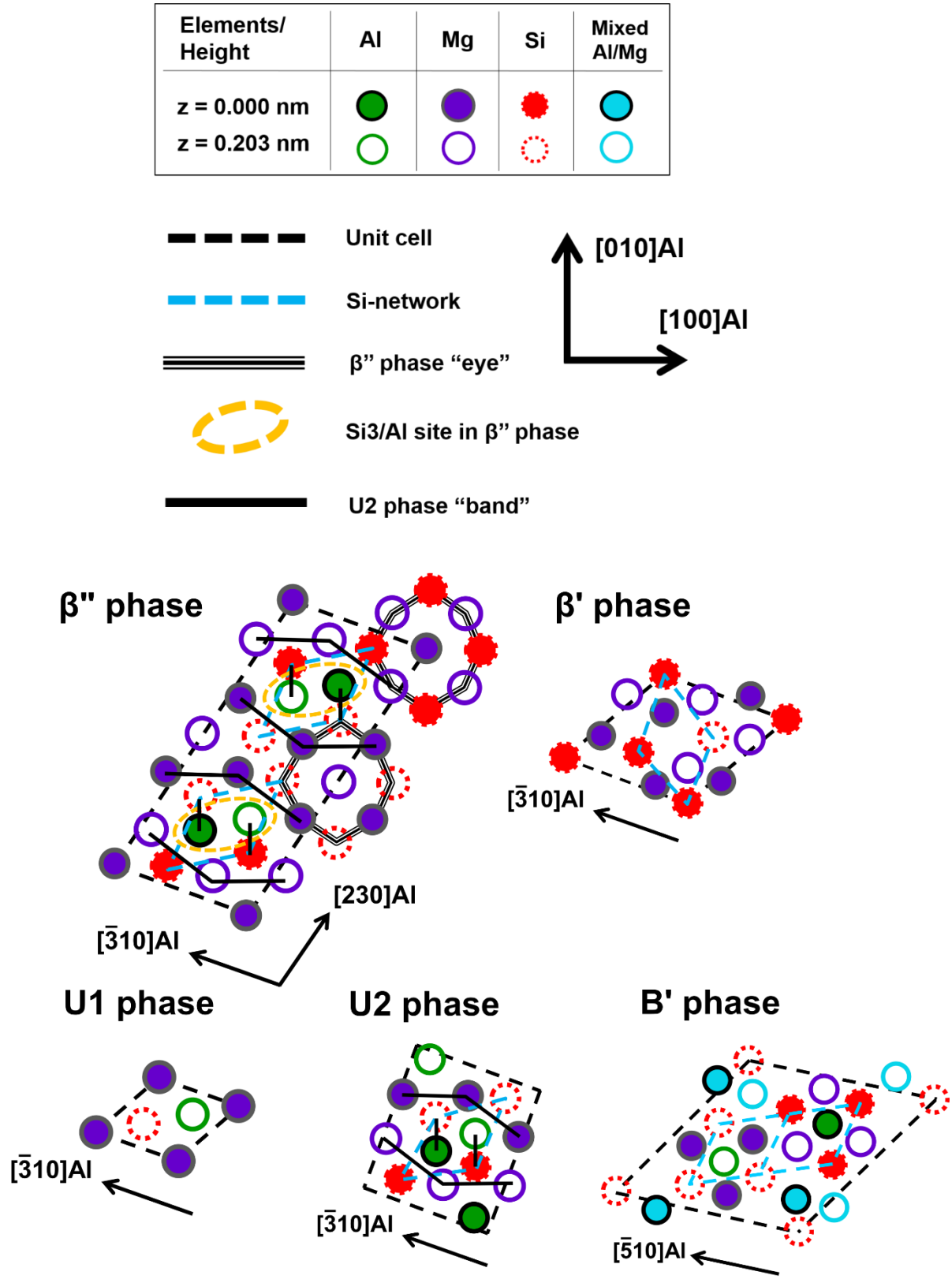

Figure 4: Structural unit cell models of metastable precipitates in Al-Mg-Si alloys drawn to the same relative scale. The composition of β” is shown as $Mg_5Al_2Si_4$. Atomic types in each atomic site of β” depend on compositions of β”. For example, if the composition of β” is $Mg_4Al_3Si_4$, the central atomic columns of "β”-eye" will be occupied by Al atoms. The structural similarities between the phases are shown through the common Si network and U2 phase "band" which connect β” and U2.

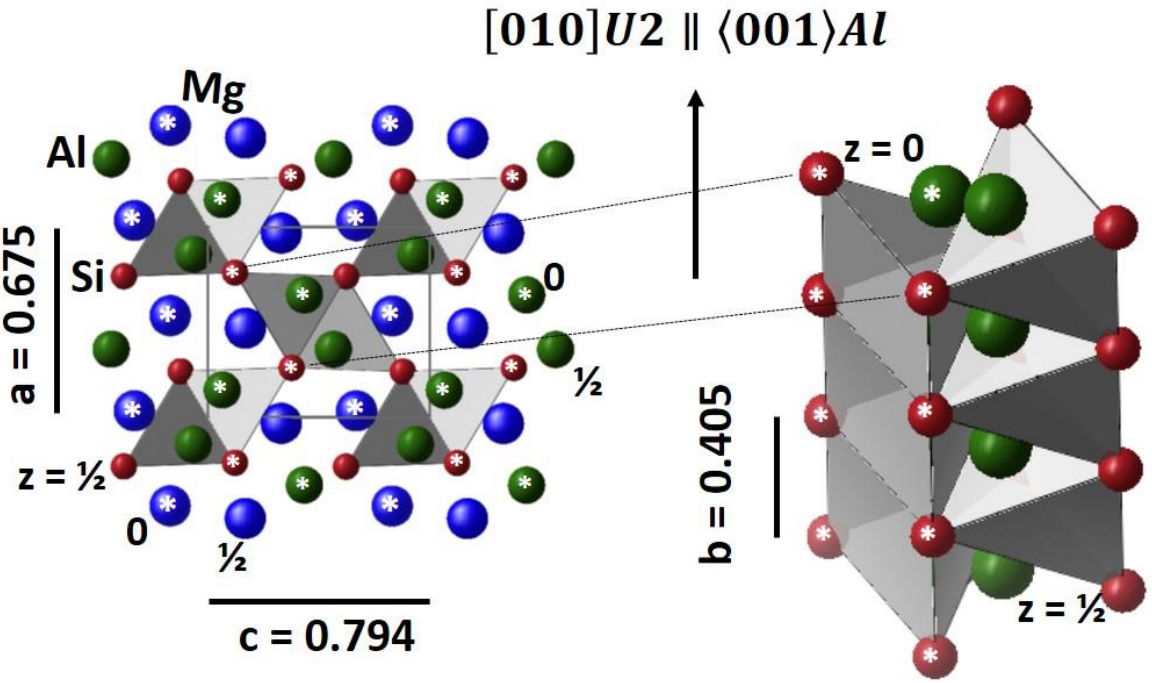

Figure 5: Left: U2–$Al_4Mg_4Si_4$ along b-axis (and <001>Al viewing direction). All Si atoms can be defined as vertices of empty pyramids. An asterisk indicates (the height of) one of the two U2 b-planes (parallel in both Al and U2), chosen as y=0. Right: Side view of the 4 central Si columns projected to two triangles (along b), showing they define rows of empty square-based Si-pyramids along <001>Al, connected edge-to-edge. Between pyramids Al atoms lie in centered Si tetrahedrons. Empty Si pyramids, connected in various ways can describe the Si-network of all precipitates including Mg_2Si and diamond silicon. The Si atoms also form pyramids and tetrahedrons around Mg.

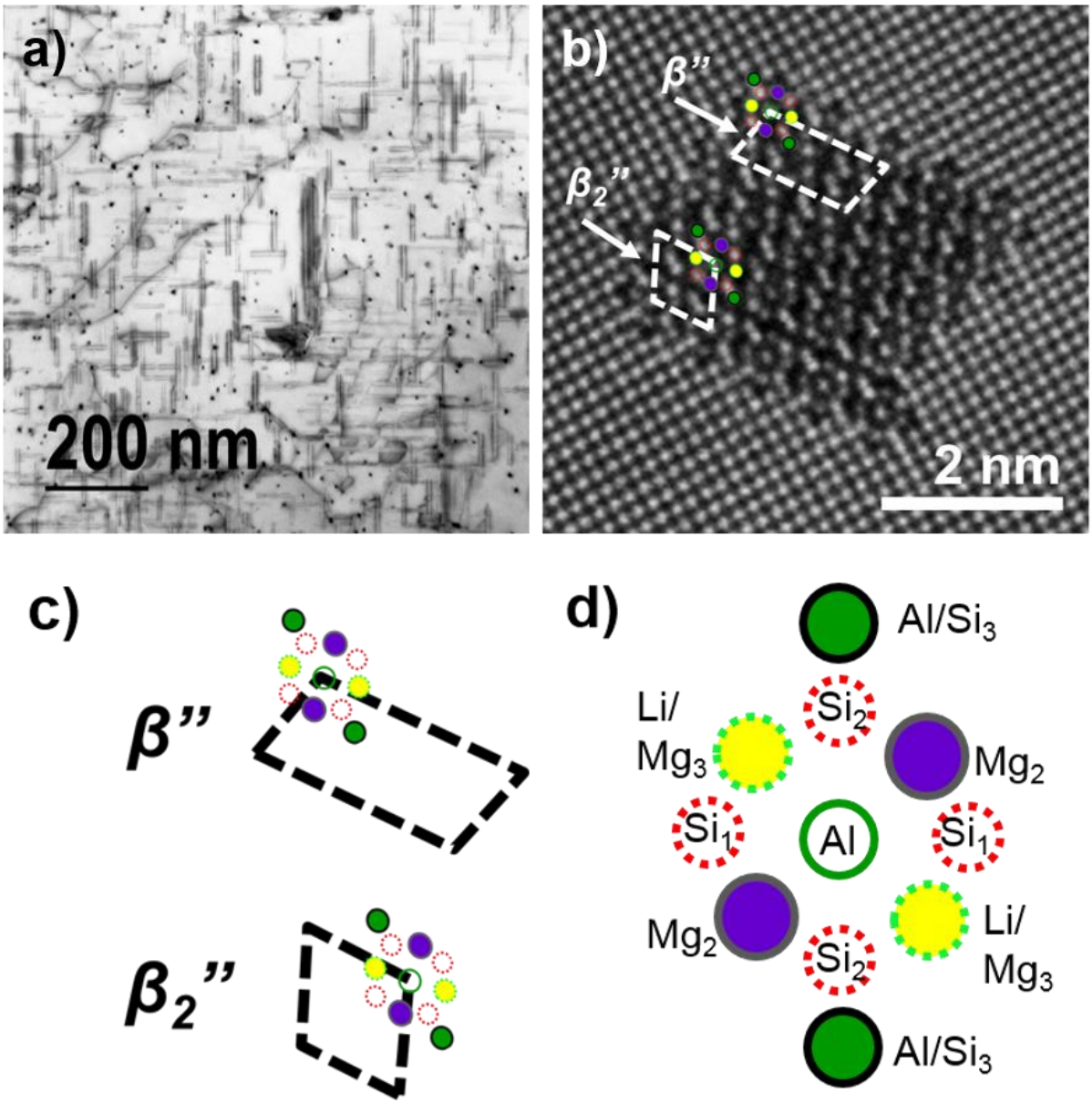

Figure 6: a) Precipitate distribution in an Al-Mg-Si-Li alloy. b) HAADF-STEM image of a precipitate cross section in an Al-Mg-Si-Li alloy with partial atomic overlay. Notice the low intensity from many Mg3-sites, indicating a higher Li-occupancy at these particular sites. A unit cell of β" and half a unit cell of β_2" is indicated by white, dashed lines. c) Enlarged views of the β" unit cell and the half unit cell of β_2" d) Model of the β"-eye with Li occupying Mg3-sites and Al at the Mg1-site in the center. The model is based on the results in [82].

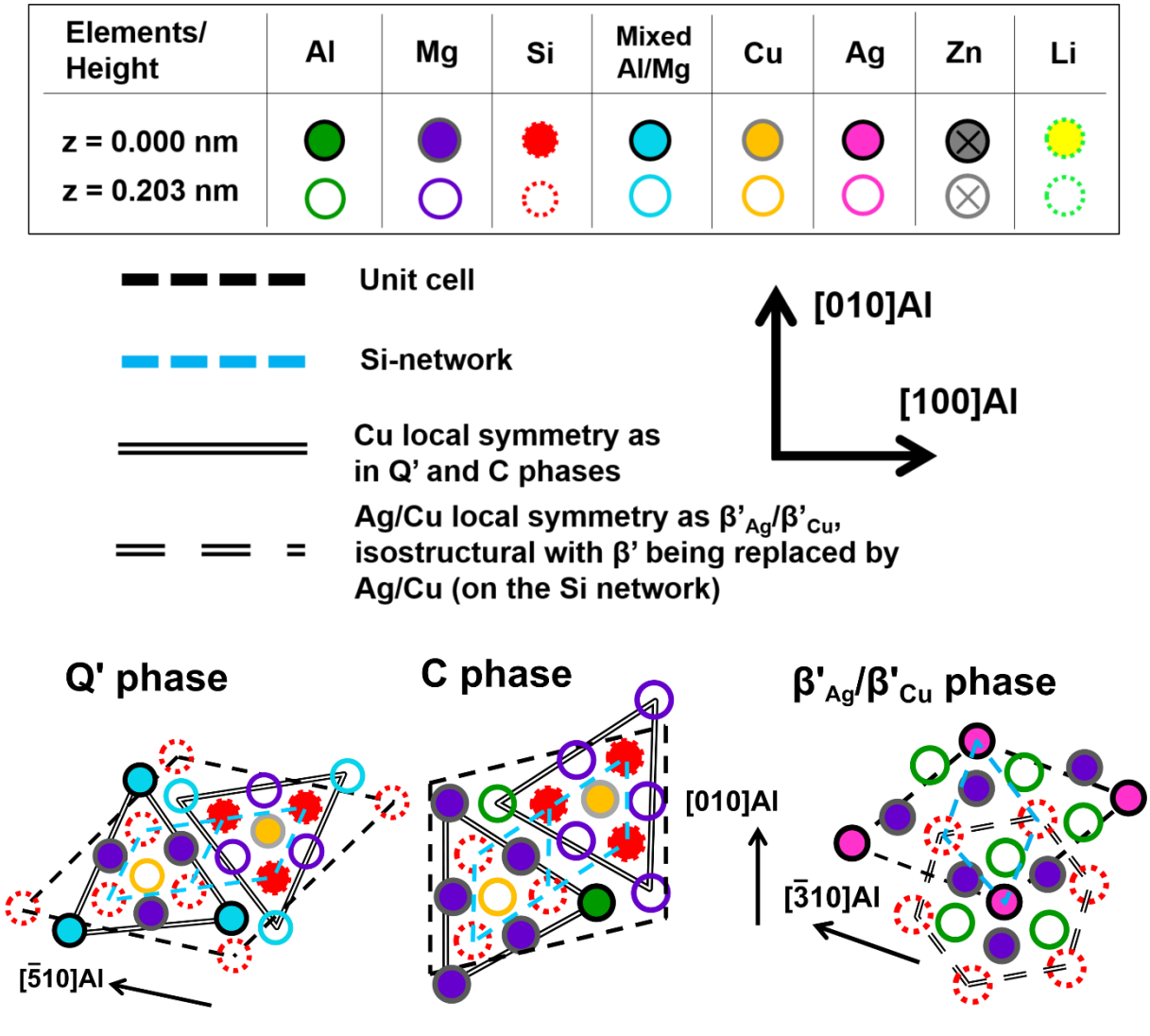

Figure 7: Structural unit cell models of Cu or Ag containing metastable precipitate phases in Al-Mg-Si alloys drawn to the same relative scale. Cu atomic columns are located in-between the Si network columns in Q' [73, 89, 93] and C phase [91] while Ag/Cu atomic columns are on the Si network in β'$_{Ag}$/β'$_{Cu}$ phase, see ref. [108, 111]. Zn atomic columns are also found in both in-between and on columns of the Si network, see section 4.3. Li atomic columns are found in the Mg3 sites of β", see Figure 6 and section 4.1.

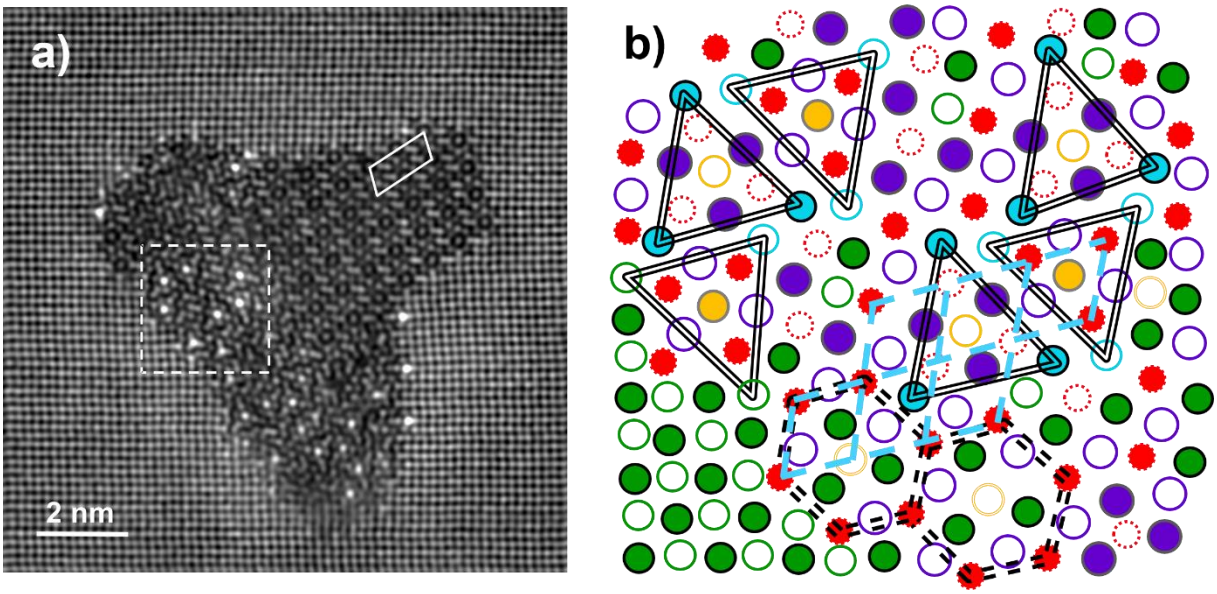

Figure 8: a) HAADF-STEM image of a Cu containing β”/disordered precipitate cross-section, and b) suggested atomic overlay of the precipitate part in the dashed white square in a). The image has been filtered using Fast Fourier transform with a circular band pass mask that removed all periods (noise) shorter than 0.15 nm. White solid line in a) shows unit cell of β”. See legend in Figure 7. Full description of the atomic overlay can be found in ref. [108].

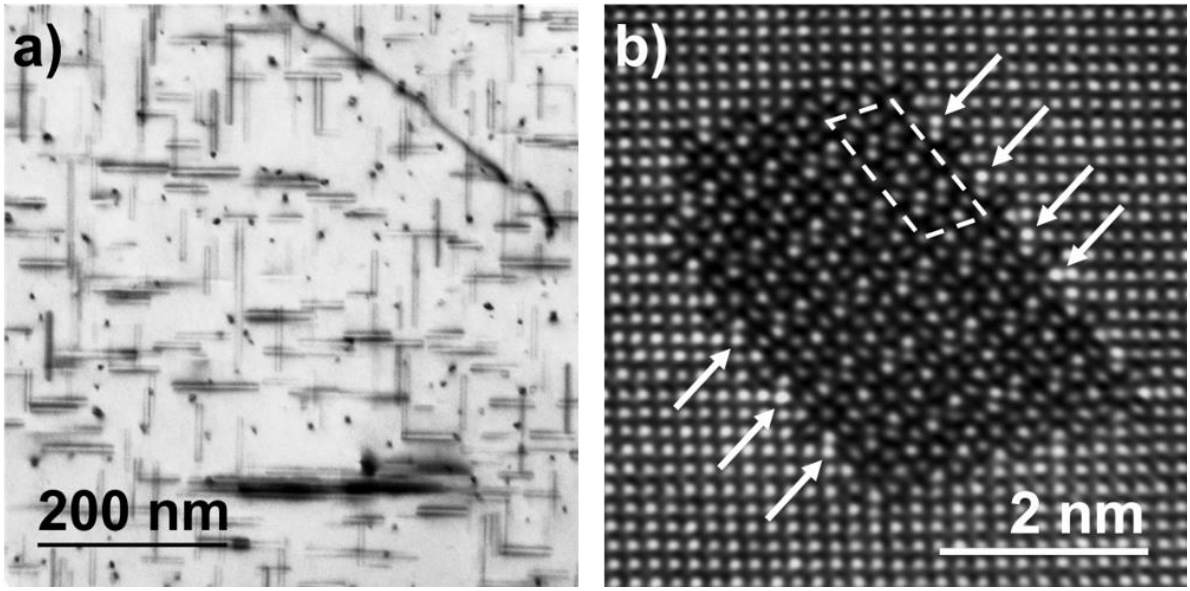

Figure 9: a) Precipitate distribution in an Al-Mg-Si-Li-Cu alloy. b) Original, unprocessed HAADF-STEM image of a precipitate cross section in an Al-Mg-Si-Li-Cu alloy. Cu atomic columns located at the precipitate/matrix interface are indicated by arrows. The white dashed lines indicate one β” unit cell [80].

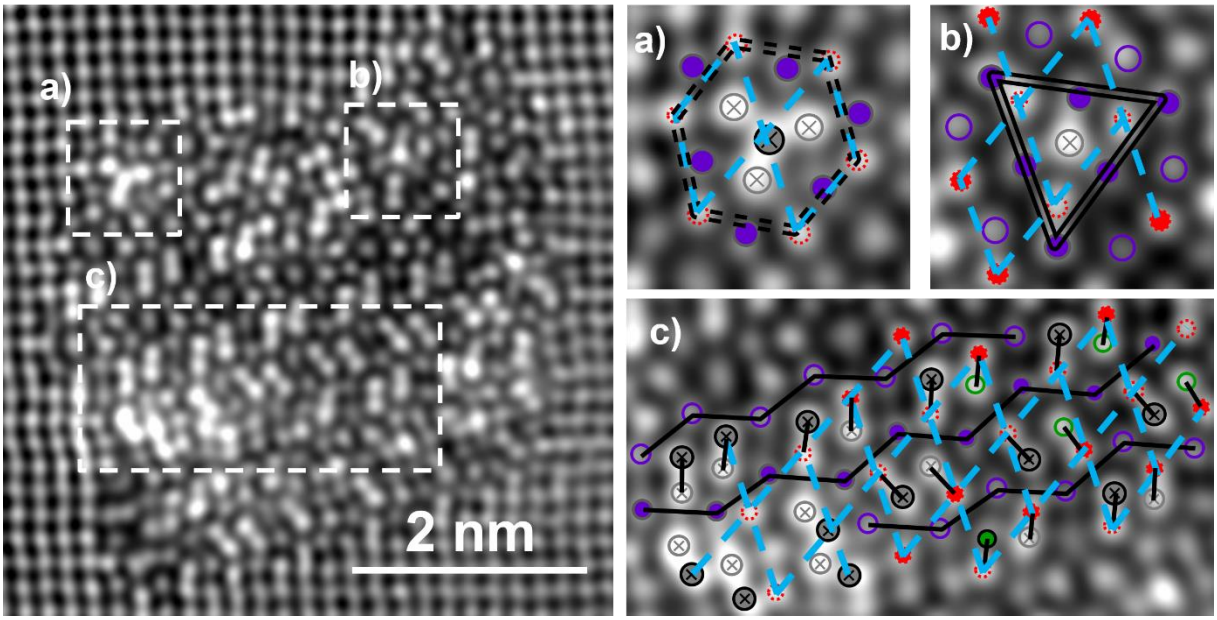

Figure 10: HAADF-STEM image of a Zn containing disordered precipitate cross-section (left), and local atomic configurations (right) shown in the areas a),b) and c) which can be identified in the β'$_{Ag}$/β'$_{Cu}$ phase [111], the C/Q' phase [91] and the U2 phase [69], respectively. The image has been filtered using Fast Fourier transform with a circular band pass mask that removed all periods (noise) shorter than 0.15 nm. See legend and the configurations in Figures 4 and 7. Full description of the atomic overlay can be found in ref. [113].

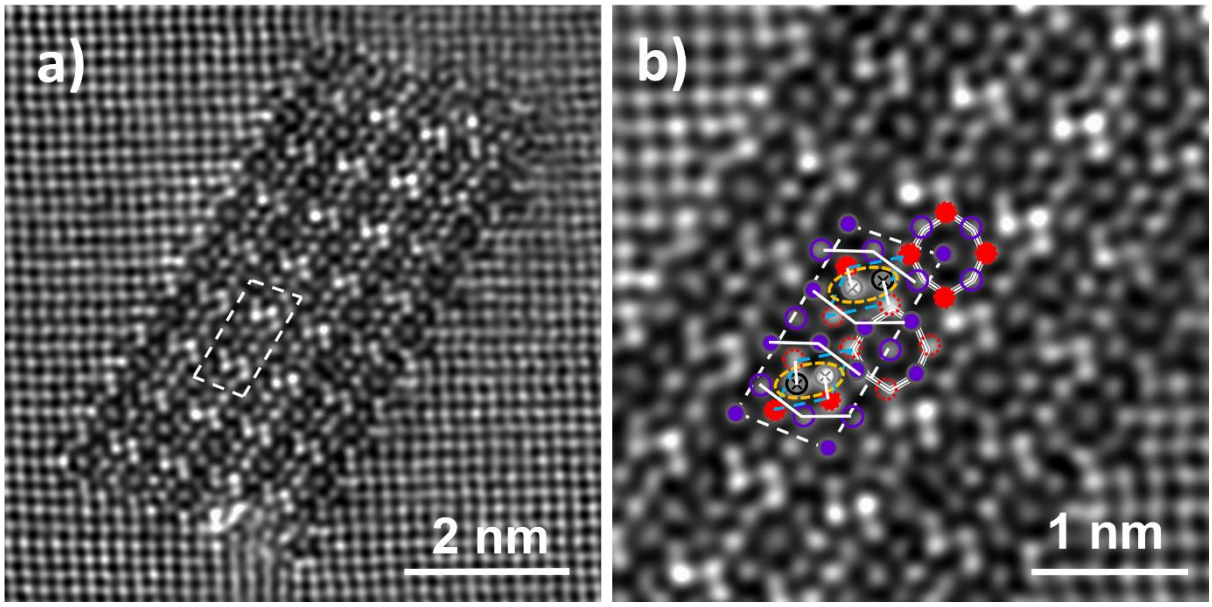

Figure 11: a) HAADF-STEM images of a β" precipitate cross section in a Zn containing Al-Mg-Si alloy showing the Zn incorporation on the Si3/Al sites, and b) enlarged part of a). The images have been filtered using Fast Fourier transform with a circular band pass mask that removed all periods (noise) shorter than 0.15 nm. See legend and the unit cell in Figures 4 and 7. Detailed analysis can be found in ref. [81].

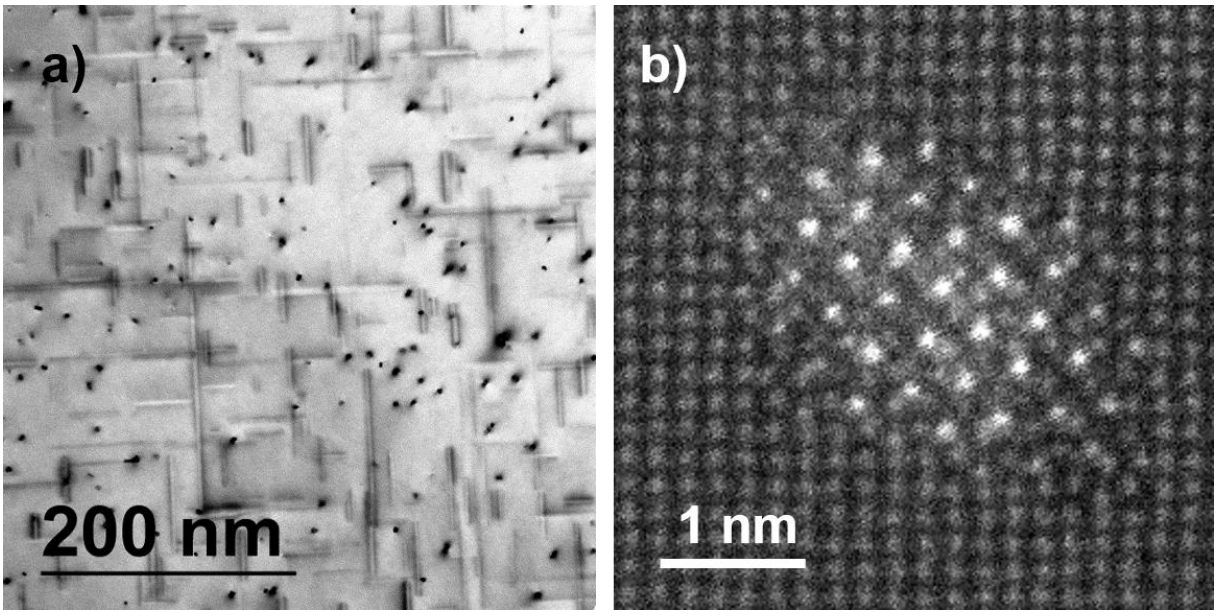

Figure 12: a) Precipitate distribution in an Al-Mg-Si-Ge alloy. b) Original, unprocessed HAADF-STEM image of a precipitate cross section in an Al-Mg-Si-Ge alloy. The Ge atomic columns are arranged in a projected hexagonal Si/Ge-network, and exhibit high contrast because of its high atomic number relative to Mg, Al and Si.

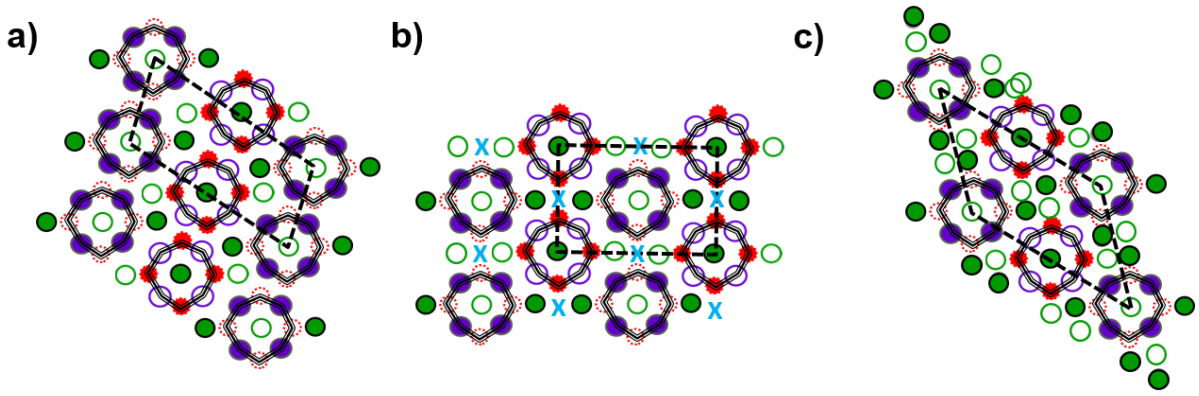

Figure 13: The three stacking variations of β'', all with two β''-eyes per unit cell. The unit cell is indicated by black dashed lines. a) Normal β'', b) β_2'', where the vacated columns are marked by X, and c) β_3''. See legend in Figure 7.

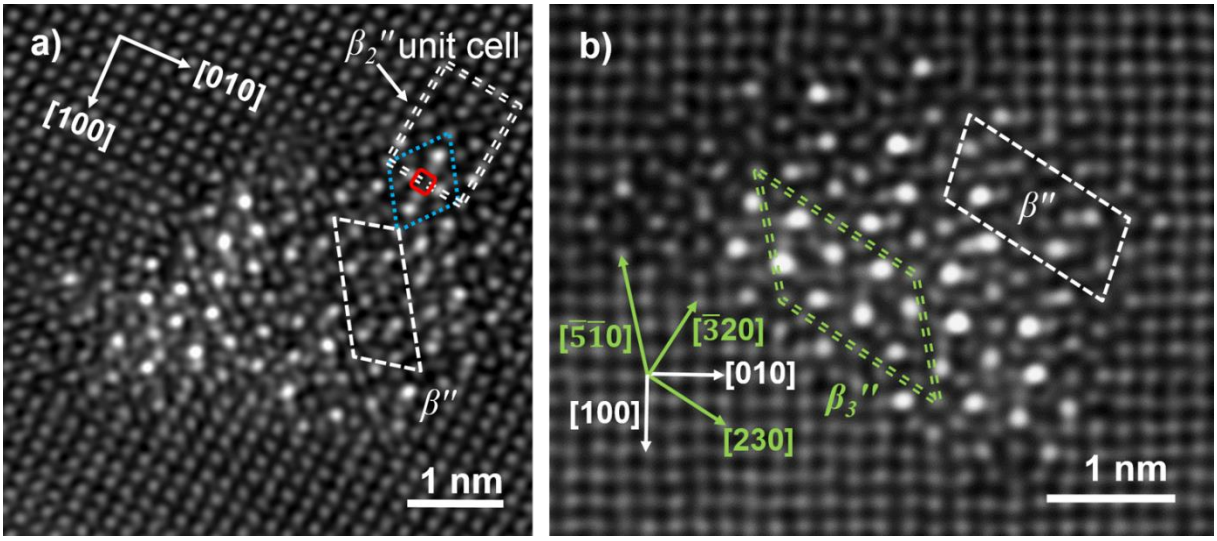

Figure 14: a) HAADF-STEM image of a cross section exhibiting both β", white dashed lines, and β_2" (double dashed lines). The vacated column is indicated by the red square. b) HAADF-STEM image of cross section exhibiting β" (white dashed lines) and β 3" (green dashed lines).

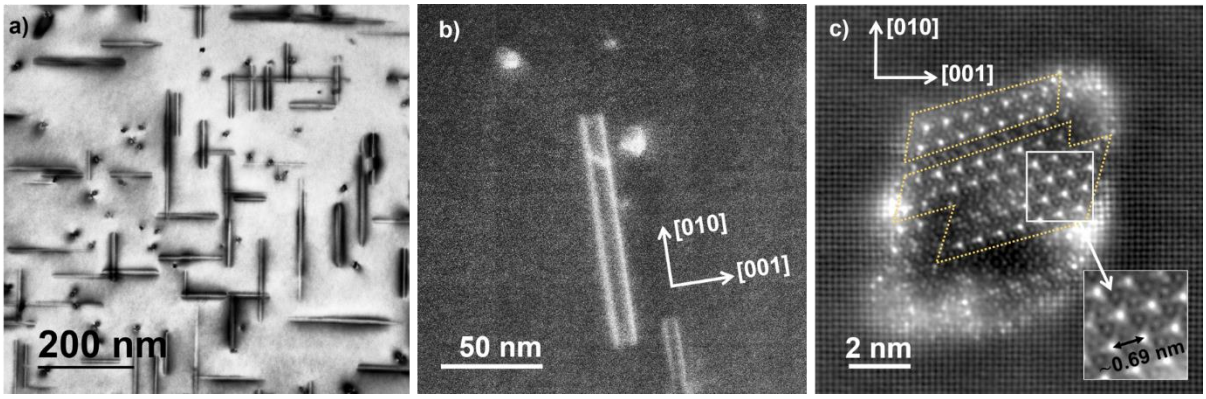

Figure 15: a) Precipitate distribution in an Al-Mg-Si-Ag-Cu alloy. b) Original, unprocessed HAADF-STEM image of needles viewed perpendicularly in the same alloy. The higher intensities at the precipitate interface corresponds to Ag. c) Unprocessed HAADF-STEM image of cross section incorporating β'_{Ag} (indicated by yellow dashed lines). The enlarged region illustrates the distance between Ag atomic columns in the hexagonal configuration. Ag enrichment of the Al-matrix adjacent to the precipitate interface is also observed.

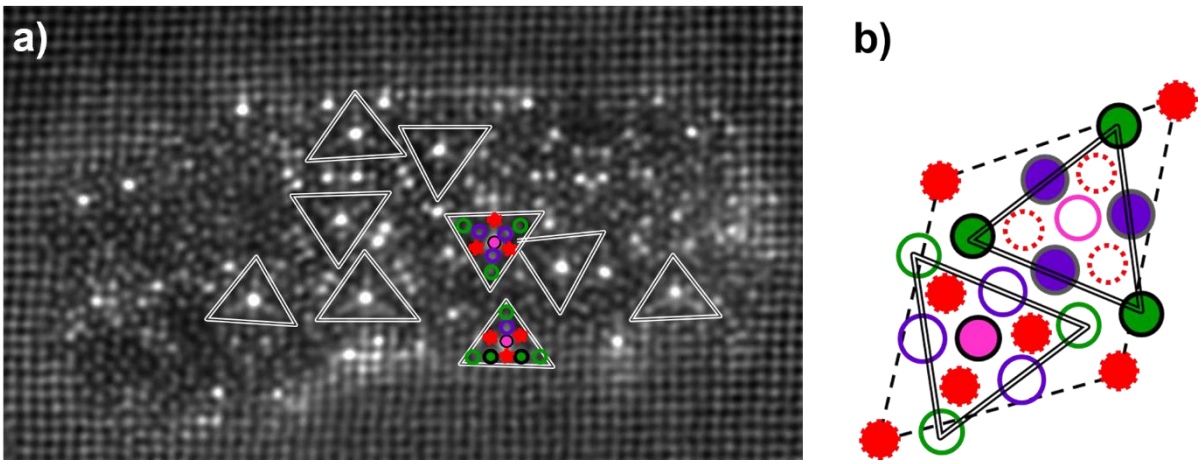

Figure 16: a) HAADF-STEM image of a cross section from an Al-Mg-Si-Ag alloy. The local Q'$_{Ag}$-configurations are indicated by double-lined triangles. b) Model of the Q'$_{Ag}$ phase which occurs in Al-Mg-Si-Ag alloys without Cu additions [37]. The model is overlayed in parts of the cross section in a). See legend in Figure 7.

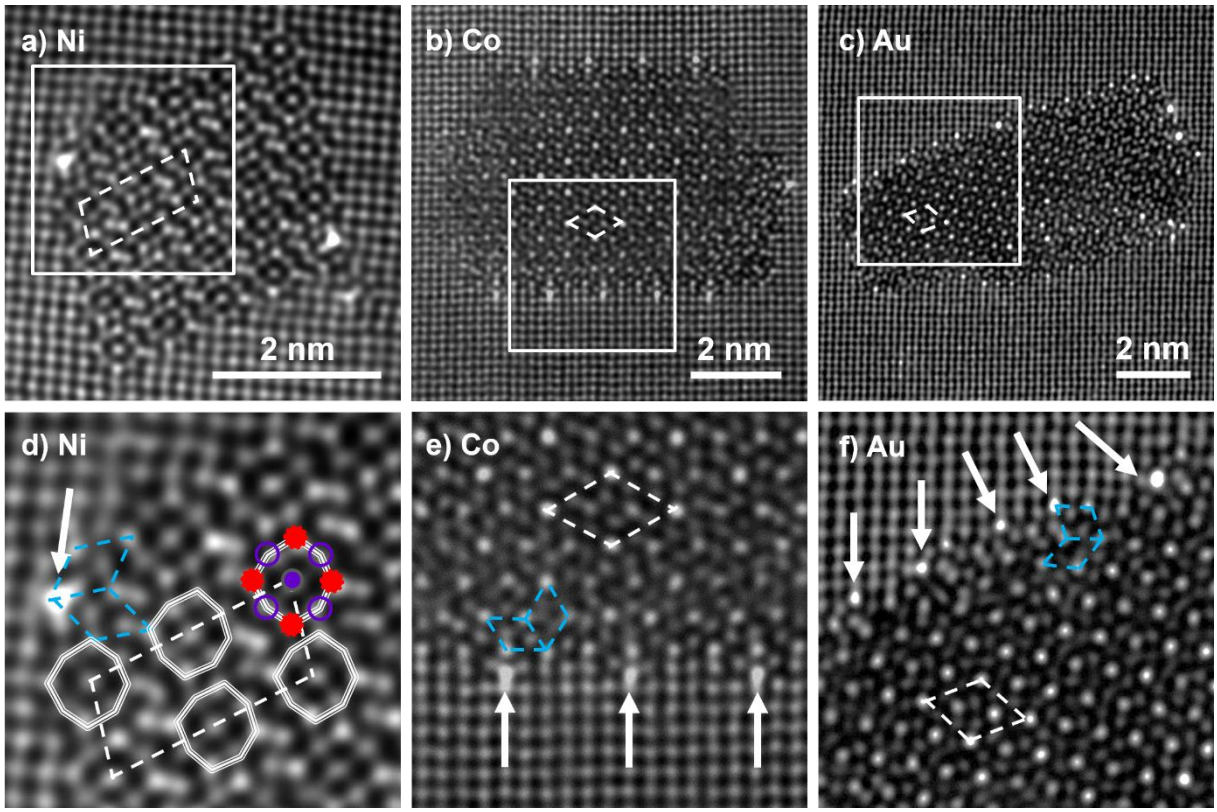

Figure 17: HAADF-STEM image of a) Ni, b) Co and c) Au containing precipitate cross sections, and d), e) and f) corresponding to the magnified images in white solid square of a), b) and c), respectively. The images have been filtered using Fast Fourier transform with a circular band pass mask that removed all periods (noise) shorter than 0.15 nm. White arrows show Ni, Co or Au containing atomic sites in each image. White dashed lines show unit cell of β'' in a) and d) and unit cell of β' in b), c), e) and f). Blue dashed lines show the Si network. See the unit cells and the legend in Figure 4.

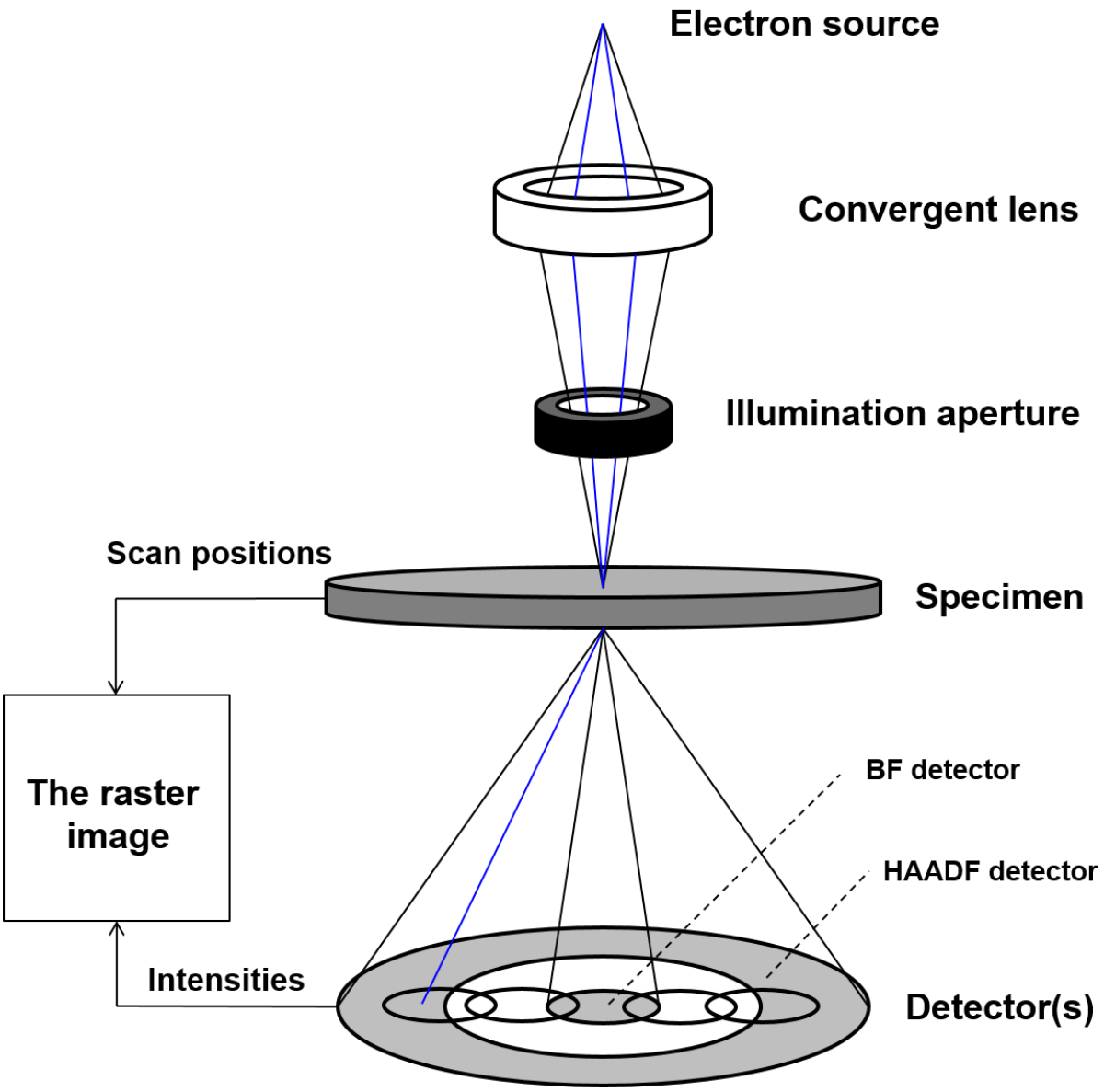

Figure 18: Schematic illustration of HAADF-STEM. The electron probe is scanned in a rectangular area in a raster over the specimen to collect intensities at each probe position. This figure is partly adapted and reproduced with permission from [131].

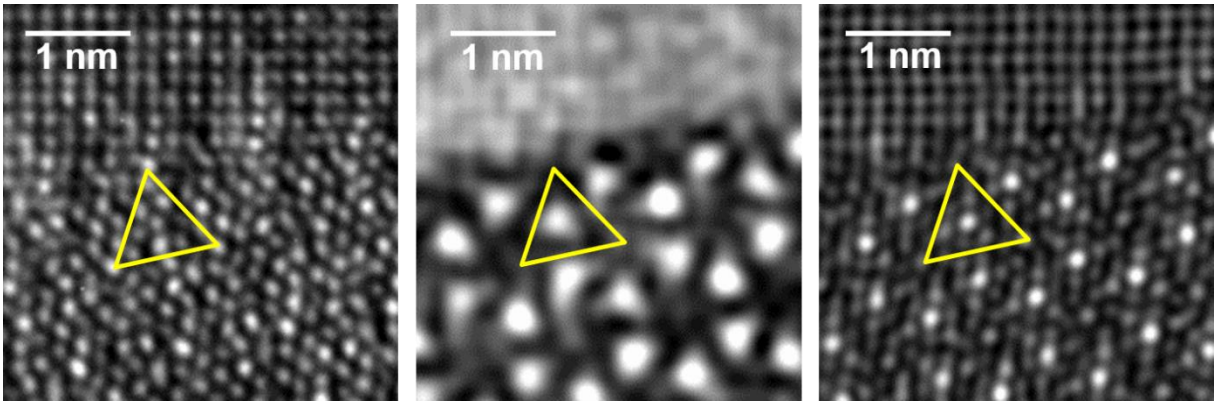

Figure 19: Q' phase shown (left) by a high resolution TEM image (phase contrast) taken by a JEOL 2010F, (middle) by a corresponding HAADF image taken at the same microscope, with Z contrast, but with limited resolution, and (right) by a probe aberration corrected image from the double corrected JEOL ARM-200CF, providing high resolution and Z contrast. All images are taken at 200 kV. See also the structural model of Q' phase in Figure 7.

Table 1. Precipitate phases encountered in Al-Mg-Si alloys.

Phases	Compositions	Space Groups	Lattice parameters [nm]
GP zones	Variable	C2/m	a = 1.48, b = 0.405, c = 0.648, β = 105.3°
β"	$Mg_{6-x}Al_{1+x}Si_4$ ($0 \leq x \leq 2$)	C2/m	a = 1.516, b = 0.405, c = 0.674, β = 105.3°
β'	$Mg_{1.8}Si$	$P6_3/m$	a = b = 0.715, c = 0.405, γ = 120°
U1	$MgAl_2Si_2$	$P\bar{3}m1$	a = b = 0.405, c = 0.674, γ = 120°
U2	MgAlSi	Pnma	a = 0.675, b = 0.405 c = 0.794
B'	$Mg_9Al_3Si_7$	Hexagonal	a = b = 1.04, c = 0.405, γ = 120°
β	Mg_2Si	$Fm\bar{3}m$	a = 0.635

Table 2: Precipitate phases encountered in Cu containing Al-Mg-Si alloys. The QP and QC phases proposed in ref. [67, 92] are probably a disordered phase connected with the Si network and the β'_{Cu} phase, respectively. See the main text.

Phases	Compositions	Space Groups	Lattice parameters [nm]
L	Variable	Disordered	-
C	$Mg_4AlSi_{3.3}Cu_{0.7}$	$P2_1/m$	a = 1.032, b = 0.405, c = 0.810, β = 100.9°
QP	Unknown	Hexagonal	Probably a disordered phase with the Si network
QC	Unknown	Hexagonal	Probably the β'_{Cu} phase
Q'	$Al_3Cu_2Mg_9Si_7$	$P\bar{6}$	a = b = 1.032, c = 0.405, β = 120°
Q	$Al_3Cu_2Mg_9Si_7$	$P\bar{6}$	a = b = 1.032, c = 0.405, β = 120°

Table 3: β'' stacking variations encountered in Ge containing Al-Mg-Si alloys [37]. D denotes a mix of Ge and Si (diamond element), and vacated columns are denoted by X.

Phases	Compositions	Space Groups	Lattice parameters [nm]
β''	$Mg_8D_8Al_6$	C2/m	a = 1.516, b = 0.405, c = 0.674, β = 105.3°
β_2''	$Mg_8D_8Al_6X_2$	C2/m	a = 1.215, b = 0.405, c = 0.810, β = 90°
β_3''	$Mg_8D_8Al_{10}$	C2/m	a = 1.516, b = 0.405, c = 1.033, β = 135°

Table 4: Precipitate phases encountered in Ag containing Al-Mg-Si alloys.

Phases	Compositions	Space Groups	Lattice parameters [nm]
β'_{Ag}	$Mg_3Al_3Si_2Ag$	$P\bar{6}2m$	a = b = 0.690, c = 0.405, γ = 120°
$(Q')_{Ag}$	$Al_3Ag_2Mg_9Si_7$	$P\bar{6}$	a = b = 1.032, c = 0.405, γ = 120°